

Hot and cloudy: High temperature clouds in super-Earths and sub-Neptunes

L. J. Janssen,¹*, Y. Miguel^{1,2}, M. Min², H. Huang³, M. Zilinskas^{2,4}, C.P.A. van Buchem¹

¹Leiden Observatory, Einsteinweg 55, 2333 CC Leiden

²SRON Netherlands Institute for Space Research, Niels Bohrweg 4, 2333 CA Leiden, The Netherlands

³Department of Astronomy, Tsinghua University, Haidian DS 100084, Beijing, China

⁴Jet Propulsion Laboratory, California Institute of Technology, Pasadena, CA, USA

Accepted XXX. Received YYY; in original form ZZZ

ABSTRACT

JWST observations provide for the first time evidence for an atmosphere on a rocky exoplanet - 55 Cnc e. The atmosphere of 55 Cnc e is hot with $T_{eq} > 2000$ K and shows strong variability, for which cloud formation above a molten crust could be one possible explanation. The composition of the atmosphere of 55 Cnc e is still unknown but suggests the presence of volatiles. We have run cloud formation models on a grid of N-dominated, O-dominated, C-dominated and H-dominated atmospheres to investigate which type of cloud we could expect on hot super-Earths and hot sub-Neptunes (1000 K < T < 3000 K). Our models combine radiative transfer with equilibrium chemistry of the gaseous and condensed phases, vertical mixing of condensable species, sedimentation, nucleation and coagulation. We find that the condensability of species is highly dependent on the oxygen abundance of an atmosphere. Oxygen poor atmospheres can be heated by UV and optical absorbers PS, TiO and CN which create temperature inversions. These inhibit condensation. Oxygen rich atmospheres are colder without temperature inversions, and are therefore more favourable environments for cloud formation. The major expected cloud component in O-dominated atmospheres with solar refractory abundance is TiO₂(s). Spectral features of clouds in these worlds are stronger in transmission than in emission, in particular at short wavelengths. We find a lack of optical data of solid species in comparison to the variety of stable cloud components which can form on hot, rocky planets.

Key words: exoplanets - planets and satellites: atmospheres - planets and satellites: composition - methods: numerical

1 INTRODUCTION

Short period planets - $P < 100$ days, which are smaller than Neptune are numerous (Fulton et al. 2017; Bean et al. 2021). A lack of planets around $1.8 R_{\oplus}$ has been observed dividing these small objects into two categories: Smaller planets $< 1.8 R_{\oplus}$ (super-Earths) and planets of $2 - 3 R_{\oplus}$ (sub-Neptunes) (e.g. Fulton et al. 2017; Izidoro et al. 2022; Burn et al. 2024). The reason for the lack of planets between $1.5 - 2 R_{\oplus}$ - the so called Radius Valley - is debated. Both, atmospheric mass loss driven by internal heating of the planet and/or by XUV flux from the star, as well as a composition gap between the two populations have been proposed as a potential cause Owen & Wu (2013); Fulton et al. (2017); Ginzburg et al. (2018); Luque & Pallé (2022). These small, hot planets are ideal candidates for studying rocky planet characteristics. Due to the proximity to their host stars, they are bright in thermal emission and have a higher transit probability compared to their temperate counterparts. Hot, rocky planets with surfaces > 1500 K are expected to be molten (van Buchem et al. 2023). We can probe the interiors of these molten planets by probing their atmospheres because material is outgassed from the magma into the atmosphere. Studying outgassed atmospheres of hot,

rocky exoplanets can teach us about different evolutionary stages of rocky planets in a more general context. Temperate rocky planets are also expected to go through a molten stage in their evolution before solidifying (Lichtenberg & Miguel 2025a).

Observations of small planets are looking more and more promising. Hu et al. (2024) have for the first time shown the existence of an atmosphere on a hot, rocky planet: 55Cnc e. Zieba et al. (2023) rule out a thick CO₂ atmosphere on TRAPPIST-1c and Ducrot et al. (2025) show that a hazy, CO₂ atmosphere is a possibility for TRAPPIST-1b. Dang et al. (2024) have obtained phase curve observations of the hot super Earth K2-141b. Ariel will allow full phase curve measurements of sub-Neptune sized planets opening up new possibilities for the understanding of their atmospheres in 3D. Additionally, JWST programs such as the Hot Rock Survey are ongoing (August et al. 2025; Meier Vald'és et al. 2025). This program targets nine hot, rocky exoplanets around M-dwarfs to reveal whether such planets can have atmospheres. The JWST Cycle 4 programme includes the Hot Rocky planet survey by Dang et al. (2025), which will provide us with an overview on which hot, rocky planets can sustain an atmosphere and inform us whether their interiors are fully molten. In the future, the Rocky Worlds DDT JWST program (Redfield et al. 2024) promises further observations of hot, rocky planets in emission.

* E-mail: ljanssen@strw.leidenuniv.nl

In such hot, environments, we can still expect some solid and liquid species to be stable. [Wakeford et al. \(2017\)](#) have shown that some high temperature condensates form at temperatures higher than 2000 K. In hot, rocky planets the availability of condensable material could be enhanced compared to gas giants because not only volatiles but also refractories such as silicon, iron, potassium, sodium, aluminium and calcium are outgassed in the form of a secondary atmosphere ([van Buchem et al. 2023, 2024; Gaillard & Scaillet 2014](#)). If some of these condensable materials form clouds, they could play an important role in controlling the climate on the planet due to clouds' effects on the gas phase composition, on the temperature profile, and on the atmospheric dynamics in planetary atmospheres ([Helling & Woitke 2006; Powell & Zhang 2024; Carone et al. 2023; Bell et al. 2024](#)). Clouds set the planetary albedo, and can in some cases create a green house effect and trap IR radiation on the planet (e.g. [Heng & Demory 2013; Helling 2019; Essack et al. 2020](#)). They affect the atmospheric composition by being sinks for certain gas phase species ([Huang et al. 2024](#), e.g.). Concerning the observational aspect, clouds can diminish the magnitude of spectral features or generate new features (e.g. [Kreidberg et al. 2014; Grant et al. 2023](#)).

In this work, we explore which solid and liquid species can be stable in atmospheres of hot, sub-Neptune sized planets, including both super-Earths and sub-Neptunes. We investigate how clouds composed of the identified species affect observations at the relevant wavelengths (0.1 – 30 μm) to prepare for the interpretation of upcoming data of current and future missions observing these planets such as JWST, Ariel and PLATO ([Gardner et al. 2006; Tinetti et al. 2018; Rauer et al. 2025](#)).

55 Cnc e is a particularly interesting case to explore, since it falls in between what is called a sub-Neptune and a super-Earth ([Hu et al. 2024](#)). Strong variability has been detected in multiple observing programs ([Dragomir et al. 2014; Demory et al. 2016; Meier Valdés et al. 2023](#)), but the cause is still unknown and the possible explanations range from volcanism, to a dust torus to a transient atmosphere ([Demory et al. 2016; Meier Valdés et al. 2023; Heng 2023](#)). A recent study by [Loftus et al. \(2024\)](#) suggests that a cyclical pattern between outgassing, cloud formation, and resulting heating of the atmosphere could be another explanation for the strong variability observed on 55 Cnc e. Cloud formation from microphysics on 55 Cnc e had been considered before by [Mahapatra et al. \(2017\)](#). They compute equilibrium chemistry of the gas phase for a hydrogen-dominated atmosphere and make use of the 1D microphysical cloud model by [Helling & Woitke \(2006\); Helling et al. \(2008\)](#). They use a temperature structure from retrievals by [Demory et al. \(2016\)](#) and find that the most stable clouds on 55 Cnc e are magnesium- and silicon- oxides. However, atmospheres of rocky planets are not necessarily H-dominated. On the contrary, [Heng et al. \(2025\)](#) suggests that the mean molecular weight of the atmosphere increases for smaller planets. Similar conclusions are also drawn by [Cherubim et al. \(2025\)](#), who show that an O₂-dominated atmosphere is the most likely composition for hot, rocky planets. If we base the conclusions of potential atmospheres of hot rocky planets on observations, the possibilities for their compositions are numerous. [Zilinskas et al. \(2025\)](#) show that good fits for spectra of the hot super-Earth 55 Cnc e taken by MIRI and NIRSpec JWST, can be nitrogen, phosphorus, carbon, oxygen and/or hydrogen dominated.

In this work, we account for the wide variety of potential atmospheric compositions of hot sub-Neptunes and super-Earths. We calculate temperature-pressure profiles self-consistently from the gas phase composition, predict which condensates can be stable in these

Table 1. Star-planet parameters of the 55 Cnc e system

parameter	value
a	0.016 AU (Bourrier et al. 2018)
R _p	1.947 R _{Earth} (Crida et al. 2018)
M _p	8.6 M _{Earth} (Crida et al. 2018)
R _s	0.98 R _{sun} (Crida et al. 2018)
T _s	5214 K (Hu et al. 2024)
P _{surf}	10 bar (Hammond & Pierrehumbert 2017)

environments and show the effect that clouds forming from these species can have on transmission spectra. In section 1, we identify the most important condensates which can be stable in atmospheres of hot sub-Neptunes and super-Earths with equilibrium chemistry. In a second step we investigate the effect of the oxygen abundance of the atmosphere on the stability of these species on the example case of 55 Cnc e. We then compare the equilibrium chemistry results with a detailed cloud formation model. We simulate transmission spectra to verify whether different cloud species would be observable and distinguishable on a planet like 55 Cnc e. In section 4, we use the cloud formation model to investigate the observability of clouds in O₂/CO₂ atmospheres. Finally, we conclude in section 5.

2 METHODS

In this paper we focus on atmospheres of hot, sub-Neptune sized planets, including both sub-Neptunes and super-Earths. For simplicity, we refer to both populations as sub-Neptunes and use the planetary system 55 Cnc e as a representative case of both populations, since its radius and density situate the planet in between ([Hu et al. 2024](#)). Parameters are listed in Table 1, to set the conditions for the radiative transfer calculations. The goal is not to model this specific planet in detail, but to use it as an illustrative example for atmospheres of hot super-Earths and hot sub-Neptunes in general.

Our pipeline contains two separate loops, as illustrated in Figure 1. The main loop is run for all our investigations and allows us to self-consistently compute the atmospheric temperature structure and equilibrium chemistry. The cloud loop and spectrum computation are only run for some selected models. With this part of the pipeline, we compute detailed cloud models to determine cloud composition, new gaseous abundances and spectral features. We explain the methodology in this section.

2.1 Radiative transfer

We compute the temperature structure of the planet with HELIOS ([Malik et al. 2017, 2019a,b; Whittaker et al. 2022](#)), accounting for absorption and scattering by species. HELIOS uses the two-stream approximation to calculate the radiative-convective equilibrium for a gas of a specified composition. We use our results from FASTCHEM3 in combination with opacities from [Zilinskas et al. \(2023\)](#) with a resolution R 2000. We account for the opacities of following gaseous species: N₂, NaO, NO, SiN, SO, HNO₃, C₂, CaOH, FeH, H₂⁺, H₃O⁺, KOH, OH⁺, SiH₂, SiH₄, SiS, N₂O, NaOH, H₂CO, CH, PC, CS, H₂O₂, NH, NS, PH, PO, SO₃, SO₂, MgH, AlH, CaH, TiH, C₂H₂, C₂H₄, Mg, SiO, AlO, CaO, SiO₂, H₂O, CO, CH₄, Al, Ca, Fe, K, MgO, Na, Si, Ti, TiO, NH₃, NaH, SiH, H₂S, S, PS, CO₂, HCN, OH, CH₃, CN, HS, PH₃, O₂, H₂, H, He, bound free and free free emission of H⁺ and collision induced absorption of H₂ – H₂. All line lists which we make use of are listed in Tables A1 and A2 with their

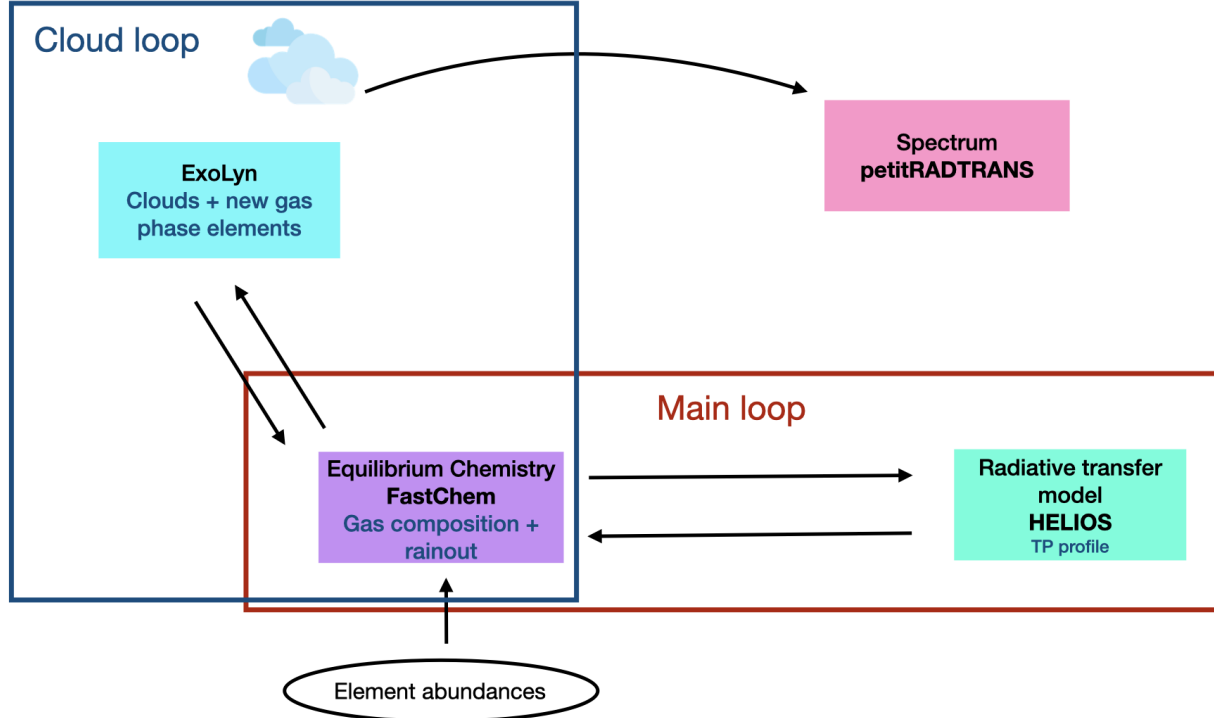


Figure 1. The sketch illustrates the different components of our pipeline. The main loop consists of self-consistent temperature profile and equilibrium chemistry computations achieved through iterations between HELIOS and FASTCHEM3. Simple rainout is used in these computations to mimic the presence of a cloud in the atmosphere. For some selected cases we run the cloud loop, where we use the output of our main loop as input for the detailed cloud model ExoLyn and recompute the gas phase again with FASTCHEM3 after cloud formation. PETITRADTRANS is called last to simulate transmission spectra from the outputs of the cloud loop.

references. We use a PHOENIX model (Husser et al. 2013) for the stellar spectrum for the host star 55 Cnc A, which we generate with the star tool provided within HELIOS. In highly opaque regions, the atmosphere can become convective. In HELIOS this is accounted for by comparing the temperature gradient to a dry adiabat in each layer of the atmosphere. If the gradient is larger, it is reduced to an adiabat. For the purpose of computing the adiabatic temperature gradient in each atmospheric layer, we assume a diatomic atmosphere.

The rocky surface of the planet is taken at 10 bar. The upper limit of the atmosphere is set at 10^{-8} bar. To take into account that the atmosphere redistributes some of the energy input from the star, we set the heat redistribution in HELIOS to $f = \frac{1}{3}$, like for the best fitting case of 55 Cnc e in Hu et al. (2024); van Buchem et al. (2024). A value of $f = \frac{1}{4}$ corresponds to full heat distribution between day and night side, and $f = \frac{2}{3}$ corresponds to all heat being confined to the day side.

2.2 Equilibrium chemistry with rainout

To obtain a self-consistent atmospheric structure, the main loop of our setup is an iterative process between radiative transfer and chemistry models Figure 1. We use HELIOS to obtain a temperature structure, then we run the chemistry code FASTCHEM3 (Stock et al. 2018; Kitzmann et al. 2024) to compute vertical mixing ratios in each atmospheric layer and feed these back to the radiative transfer model. We repeat this until convergence is reached.

With the equilibrium chemistry code FASTCHEM3 (Stock et al. 2018; Kitzmann et al. 2024) we compute the abundances of 203 gas

species and ions and 109 condensates in the atmosphere for a grid of compositions from element abundances of the 18 elements H, He, N, C, P, Cl, S, V, O, Na, Mg, Si, Fe, Al, K, Ca, and Ti. The initial conditions of our pipeline are set by running FASTCHEM3 on a wide grid of temperatures and pressures between 400 – 6000 K and 10^{-8} – 1000 bar. In this grid, condensation is computed at each temperature-pressure point independently providing a first guess of the chemistry to obtain a temperature structure with HELIOS. This temperature structure is then used as a new input to FASTCHEM3 to obtain vertical mixing ratios of all included species in the atmosphere. In this part of the iterative loop, we proceed with "rainout" modelling. This approach is optional in the FASTCHEM3 code. It consists in condensation from high to low pressures, such that material condenses out layer by layer, where it is taken out of the atmosphere above. This changes the elemental budget at each altitude.

To help with convergence, we implement a gradual relaxation, by only allowing a 30% of the predicted change in temperature structure from one iteration to the other. We consider a model as converged when the maximal temperature difference between two iterations is on the order of 10 K. This relaxation method prevents the model from oscillating between hot, cloud-free cases and colder, cloudy cases.

2.3 The cloud model

Equilibrium chemistry provides an indication on the stability of solid and liquid species and can be used as a first guess for the extent and the location of cloud formation. However, disequilibrium

Table 2. Cloud formation parameters

parameter	value
σ_{mol} (molecular cross section)	$2 \cdot 10^{-15} \text{ [cm}^2]$
f_{stick} (sticking probability)	1
f_{coag} (coagulation probability)	1
σ_{com} combined cross section for vapour and H_2	$8 \cdot 10^{-15} \text{ [cm}^2]$
ρ_{int} particle internal density	$2.8 \text{ [g cm}^{-3}]$
a_{p0} (nucleation radius)	10^{-7} [cm]
m_{n0} nucleation mass	$\frac{4}{3}\pi \cdot \rho_{\text{int}} \cdot a_{p0}^3 \text{ [g]}$
Σ_n (nuclei production rate)	$10^{-15} \text{ [g cm}^{-2} \text{ s}^{-1}]$
σ_n (width nucleation profile)	0.2
P_n (nucleation height)	$60 \text{ [g cm}^{-2} \text{ s}^{-1}]$

processes are crucial to include for two major reasons:

1) Rainout chemistry underestimates the cloud mass, because at each atmospheric layer material is taken out of the atmosphere when it rains out. No replenishment from vertical movement in the atmosphere is taking place without including dynamics.

2) Equilibrium chemistry does not provide an estimate of the cloud particle size, but only the condensate abundance. To form cloud particles, nucleation, coagulation, vertical transport, and settling are required in addition to condensation and evaporation processes.

Hence, for some selected cases we use a detailed cloud model for comparison, running the cloud loop Figure 1 after completion of the main loop. We predict cloud formation in atmospheres of hot, rocky sub-Neptunes with ExoLYN (Huang et al. 2024). ExoLYN solves vertical transport for gas and solid species, computes condensation from a pure gas phase and takes into account coagulation and nucleation to compute a vertical distribution of the cloud’s mass mixing ratio and grain sizes. The model takes as input the gas phase abundance of all cloud forming species at the bottom of the atmosphere, a temperature-pressure structure, an eddy diffusion parameter K_{zz} , a particle diffusion parameter K_p , nucleation parameters to compute the nucleation profile according to Ormel & Min (2019), and cloud forming reactions. ExoLYN follows the Bruggemann model (Huang et al. 2024; Kiefer et al. 2024), assuming one particle size per cloud layer. In the Bruggemann model, each cloud particle is a mixture of all condensing material in the layer.

We use the temperature structure from our radiative transfer calculations with HELIOS and run FASTCHEM with rainout to compute the gas phase abundances at the bottom of the atmosphere. Rainout is implemented here to account for the material which remains at the surface in solid or liquid form. We keep nucleation parameters as in Huang et al. (2024) shown in Table 2. Nucleation is parameterised in ExoLYN with a lognormal nucleation profile as in Ormel & Min (2019). We note that the chosen values for nuclei production rate, width of the nucleation profile and nucleation height affect the extent of the cloud and the particle size. However, these parameters are very uncertain and are dependent on the cloud species and on the temperature (e.g. Gao et al. 2020). In addition, Huang et al. (2024) find that the nucleation profile is not the dominating factor determining the cloud profile. Therefore, we keep their default values. We set our default value for eddy diffusion for gas and solid particles to $K_{zz} = 10^{10} \text{ cm}^2 \text{s}^{-1}$ and $K_p = 10^{10} \text{ cm}^2 \text{s}^{-1}$. For the mean molecular weight of the atmosphere m_{gas} , we take an average of the mean molecular weight over the entire pressure range.

ExoLYN takes as input only one reaction per condensate. It is crucial to be careful when picking the reaction rates for condensate formation because the stability of a condensate is strongly dependent on the reaction rate and the amount of available elements to condense. For the condensates for which reaction rates are available in the literature we have considered reaction rates from Helling & Woitke (2006); Helling et al. (2008, 2017); Huang et al. (2024) and settled on the optimal choice resulting in the highest condensate mass. For the species for which condensation reactions are not available from literature, we have evaluated different reactions with combinations of reactants from the most abundant gas-phase species containing the elements required to form the condensate and have also settled on the optimal choice. The resulting condensation reactions which we consider are listed in Table 3.

2.4 Cloud features in transmission spectroscopy

To assess whether potential clouds would affect observations of hot sub-Neptunes, we first of all investigate potential features of the cloud species for which we have optical data. We then simulate transmission spectra for some selected cases between $0.1 - 30 \mu\text{m}$. We collect the refractive indices of the solid species which appear in our models and are available from either the JENA database of optical constants¹ or already implemented into ExoLYN from Kitzmann & Heng (2018). Table 4 lists all the references for the opacities of solid species relevant for this work. We then use OPTOOL (Dominik et al. 2021) to predict extinction coefficients for each of these species. Cloud particles are not expected to be perfectly spherical and their geometry affects scattering and absorption properties. Therefore, we assume a distribution of hollow spheres (DHS) to generate the cloud opacities. For solid particle agglomerations like clouds, DHS is a good approximation to model grain-light interactions (Min et al. 2005).

In a first part, we predict extinction coefficients for each solid species from Table 4 between $0.1 - 1000 \mu\text{m}$ and model the extinction of small particles with a diameter of $0.01 \mu\text{m}$ composed of one single material. In a second part, we study the effect of cloud opacities for the same selected cases which we choose for the cloud study described in section . For this investigation we run the entire cloud loop, including rainout within the equilibrium chemistry model and transmission spectra as illustrated in Figure 1. Rainout is important to account for in this case because some material which is liquid or solid already at the magma ocean pressure would rain out immediately without ever reaching the cloud formation layer. After the cloud computation with ExoLYN, we recompute the atmospheric gas chemistry with FASTCHEM3 from the remaining elements to get the mixing ratios of major gas phase molecules.

We generate cloud opacities with OPTOOL from grain sizes computed with ExoLYN and the relative mass fractions of the different components in the cloud particles. We run petitRADTRANS (Mollière et al. 2019) to predict transmission and emission features of the cloudy atmosphere, investigating a pressure range of the atmosphere from $10-10^{-8} \text{ bar}$ with the temperature structures from our radiative transfer computations. We use gas phase line by line opacities for the spectra modelling in petitRADTRANS from the ExoMol data base (Tennyson et al. 2024) at resolution $\lambda\Delta\lambda = 1000$ for the following species: Ti^+ , TiO , TiH , Ti , SO , SO_2 , SO , SiS , SiO_2 , SiO , SiH_4 , SiH_2 , SiH , Si , SH , PS , PO , PN , PH_3 , PH , OH , COS , O_3 , O_2 , O , NO , NH_3 , NH , NaOH , NaH , Na , N_2O , MgO , MgH , Mg , K , HNO_3 , HCN , H_3O^+ ,

¹ <https://www.astro.uni-jena.de/Laboratory/OCDB/index.html>

Table 3. Condensation reactions¹

Cloud species	Formation reaction
$\text{SiO}_2(\text{s})$	O-dominated atmosphere $\text{SiO} + \text{H}_2\text{O} \longrightarrow \text{SiO}_2(\text{s}) + \text{H}_2$
$\text{TiO}_2(\text{s})$	$\text{TiO}_2(\text{g}) \longrightarrow \text{TiO}_2(\text{s})$
$\text{MgTi}_2\text{O}_5(\text{s})$	$\text{Mg}(\text{OH})_2 + 2\text{TiO}_2 \longrightarrow \text{MgTi}_2\text{O}_5(\text{s}) + \text{H}_2\text{O}$
$\text{Mg}_2\text{TiO}_4(\text{s})$	$\text{Mg}(\text{OH})_2 + \text{TiO}_2 \longrightarrow \text{Mg}_2\text{TiO}_4(\text{s}) + 2\text{H}_2\text{O}$
$\text{MgSiO}_3(\text{s})$	$\text{Mg}(\text{OH})_2 + \text{SiO} \longrightarrow \text{MgSiO}_3(\text{s}) + \text{H}_2$
$\text{Mg}_2\text{SiO}_4(\text{s})$	$2\text{Mg}(\text{OH})_2 + \text{SiO} \longrightarrow \text{Mg}_2\text{SiO}_4(\text{s}) + \text{H}_2\text{O} + \text{H}_2$
$\text{MgAl}_2\text{O}_4(\text{s})$	$\text{Mg}(\text{OH})_2 + 2\text{HAIO}_2 \longrightarrow \text{MgAl}_2\text{O}_4(\text{s}) + 2\text{H}_2\text{O}$
$\text{Fe}_2\text{O}_3(\text{s})$	$2\text{FeO} + \text{H}_2\text{O} \longrightarrow \text{Fe}_2\text{O}_3(\text{s}) + \text{H}_2$
$\text{Fe}_3\text{O}_4(\text{s})$	$3\text{FeO} + \text{H}_2\text{O} \longrightarrow \text{Fe}_3\text{O}_4(\text{s}) + \text{H}_2$
$\text{FeO}(\text{s})$	$\text{FeO} \longrightarrow \text{Fe}_3\text{O}_4(\text{s})$
$\text{Fe}_2\text{SiO}_4(\text{s})$	$2\text{FeO} + \text{SiO} + \text{H}_2\text{O} \longrightarrow \text{Fe}_2\text{SiO}_4(\text{s}) + \text{H}_2$
$\text{CaSiO}_3(\text{s})$	$\text{Ca}(\text{OH})_2 + \text{SiO} \longrightarrow \text{CaSiO}_3(\text{s}) + \text{H}_2$
$\text{CaTiO}_3(\text{s})$	$\text{Ca}(\text{OH})_2 + \text{TiO}_2 \longrightarrow \text{CaTiO}_3(\text{s}) + \text{H}_2\text{O}$
$\text{Mg}_3(\text{PO}_4)_2(\text{s})$	$3\text{Mg}(\text{OH})_2 + 2\text{PO}_2 \longrightarrow \text{Mg}_3(\text{PO}_4)_2(\text{s}) + 2\text{H}_2\text{O} + \text{H}_2$
$\text{CaMg}(\text{SiO}_3)_2(\text{s})$	$\text{Ca}(\text{OH})_2 + \text{Mg}(\text{OH})_2 + 2\text{SiO} \longrightarrow \text{CaMg}(\text{SiO}_3)_2(\text{s}) + 2\text{H}_2$
C-dominated atmosphere	
$\text{Fe}(\text{s})$	$\text{Fe} \longrightarrow \text{Fe}(\text{s})$
$\text{Al}_2\text{O}_3(\text{s})$	$2\text{Al} + 3\text{H}_2\text{O} \longrightarrow \text{Al}_2\text{O}_3(\text{s}) + 3\text{H}_2$
$\text{C}(\text{s})$	$\text{O}_2\text{H}_2 \longrightarrow 2\text{C}(\text{s}) + \text{H}_2$
$\text{TiC}(\text{s})$	$\text{CH}_4 + \text{TiO} \longrightarrow \text{TiC}(\text{s}) + \text{H}_2\text{O} + \text{H}_2$

¹ Condensation reactions for each solid species in our cloud formation model. These pathways are chosen according to the availability of reactants and their efficiency to produce condensates.

Table 4. References for optical constants of solid species

solid material	source for optical data
$\text{Al}_2\text{O}_3(\text{s})$	Koike et al. (1995)
$\text{C}(\text{s})$	Draine (2003)
$\text{CaTiO}_3(\text{s})$	Palik (1991)
$\text{Fe}(\text{s})$	Palik (1991)
$\text{Fe}_2\text{O}_3(\text{s})$	A.H.M.J. Triaud
$\text{Fe}_2\text{SiO}_4(\text{s})$	Fabian et al. (2001)
$\text{FeO}(\text{s})$	Henning et al. (1995)
$\text{FeS}(\text{s})$	Pollack et al. (1994)
$\text{Mg}_2\text{SiO}_4(\text{s})$	Jäger et al. (2003)
$\text{MgSiO}_3(\text{s})$	Jäger et al. (2003)
$\text{MgAl}_2\text{O}_4(\text{s})$	Jäger et al. (2003)
$\text{MgO}(\text{s})$	Palik (1991)
$\text{SiC}(\text{s})$	Laor & Draine (1993)
$\text{SiO}(\text{s})$	Palik (1985)
$\text{SiO}_2(\text{s})$	Palik (1985); Henning & Mutschke (1997) Zeidler et al. (2013)
$\text{TiC}(\text{s})$	Henning & Mutschke (2001)
$\text{TiO}_2(\text{s})$	Posch et al. (2003); Zeidler et al. (2011)

H_2S , H_2CO , H_2 , FeH , Fe , Fe^+ , CP , CO_2 , CO , CN , CH_4 , CaOH , CaO , CaH , C_2H_4 , C_2H_2 , C_2 , AlO , AlH , AlF , Al , N_2 , He , e^- , H^- and H . In addition we include rayleigh species H_2 and He as well as continuum opacities from $\text{H}_2\text{-H}_2$, $\text{H}_2\text{O-H}_2\text{O}$, $\text{N}_2\text{-O}_2$, $\text{N}_2\text{-N}_2$, $\text{O}_2\text{-O}_2$, $\text{N}_2\text{-He}$ and $\text{H}_2\text{O-N}_2$. For the line lists used and there references see Table A1 and Table A2.

2.5 The grid of compositions

During planet formation, volatiles get trapped into a rocky planet's interior. Due to outgassing, secondary atmospheres composed of these volatiles as well as more heavy elements such as Si, Fe, Mg,

Na and K can build up around the planet (e.g. van Buchem et al. 2023, 2024; Cherubim et al. 2025; Lichtenberg & Miguel 2025b). Some of the sub-Neptune sized planets might also have a primary hydrogen envelope into which the outgassed material is mixed (e.g. van Buchem et al. 2024; Cherubim et al. 2025). Therefore, the expected compositions span a wide variety. Our aim in this work is to cover such a variety in atmospheric compositions, focusing on how different ratios of volatiles would impact condensation and cloud formation. For this purpose, we construct a grid of models with 144 different sets of element abundances.

We vary the ratios of the volatile species carbon (C), hydrogen (H), nitrogen (N), oxygen (O), phosphorus (P) and sulphur (S) while keeping all other elements in solar abundances relative to each other and relative to the total volatile content. We take these solar values from Lodders (2019). We divide our models into three types of atmospheres: N-dominated atmospheres, atmospheres that are either C- CO- or O-dominated, and H-dominated atmospheres. This choice is motivated by the different atmospheric scenarios proposed by Hu et al. (2024); Zilinskas et al. (2020, 2023). From these 3 atmospheric types we create a set of 9 (3x3) models, for which the fraction of the dominating volatile X_H , X_C X_O or X_N , varies from 60% to 75% to 90%. We explore C/O ratios 0.1, 0.5, 1 and 2, expanding this grid to a 3x3x4 grid of models. We note that these C/O ratios are taken regarding the bulk composition. Condensation and cloud formation can alter the C/O ratio of the gas phase. The carbon- and oxygen- dominated atmospheres are O-atmospheres if C/O<1, CO-atmospheres if C/O=1 and C-atmospheres if C/O>1.

The sulphur and phosphorus content of rocky planets can also be expected to vary drastically due to different sulphur and phosphorus budgets in stars (Hinkel et al. 2014), formation mechanisms and processes like outgassing and volcanism which can enhance the abundance of these volatiles as it is the case on Io (Lellouch et al. 2007; Gaillard & Scaillet 2014; van Buchem et al. 2024). In order to account for these various conditions, we explore a sulphur and phos-

phorus rich case (P+S rich) and a sulphur and phosphorus poor case (P+S poor) for each of the models in the 3x3x4 grid above, extending it to a 3x3x4x2 grid with 72 models. The P+S poor cases have abundances X_S X_P 0.1 ppm and the P+S rich cases have enhanced sulphur and phosphorus fractions of X_S X_P 1 %. For reference, solar abundances are X_S $1.7 \cdot 10^{-5}$ and X_P $3.3 \cdot 10^{-7}$ (Lodders 2019). So far, we have attributed the sulphur and phosphorus abundance as well as the abundances of the major volatile. For each model to include all species and fill up to a fraction of unity, we attribute the leftover fraction to the two leftover volatiles in a systematic way. The smallest volatile fraction among X_H , X_C , X_O and X_N is set to X_ϵ 0.01. The last leftover species is assigned an abundance such that the total fraction $X_H X_C X_O X_C X_O X_N$ 1. To summarise, we have assigned the abundance of the major volatile, the sulphur abundance and the phosphorus abundance. The least abundant volatile in the grid except for sulphur and phosphorus is assigned a fraction of X_ϵ 0.01. Since the total of $X_H X_C X_O X_C X_O X_N$ 1, we then determine the elemental abundance of the remaining volatile - or volatiles in the cases where it is C+O which we are missing - by filling up the total fraction to unity.

2.6 How oxygen abundance affects condensation

The grid study presented above covers a wide range of atmospheric oxygen abundances. In a second exploration, we focus on the effect that the oxygen abundance has on condensation. For this purpose we focus on one particular example, which is the carbon richer model of 55 Cnc e from van Buchem et al. (2024). It is to note, that this composition is not carbon rich, but van Buchem et al. (2024) refer to it as the carbon rich case since they explore another case as well which is even poorer in carbon.

We introduce this new composition in this section for a more reliable example study. The compositions explored in previous section were a purely explorative parameter study. However, in order to make predictions which are relevant for potentially observable exoplanet compositions, we now base our more detailed investigations on self-consistent models which were selected from fits to data of JWST observations by van Buchem et al. (2024); Hu et al. (2024).

The atmosphere by van Buchem et al. (2024) is H-dominated with a C/O ratio of 0.133. We then further consider four carbon- and oxygen-enriched cases of this atmosphere by increasing the O/H ratio, while keeping the C/O ratio and the N, P and S- abundances constant. Figure 2 illustrates how this changes the elemental composition of the atmosphere for each of the 5 cases. All bulk refractory abundances are taken to be solar relative to each other and relative to the total volatile content, similar to our grid study described in section 2.5.

3 RESULTS

In this section we explore which cloud species we can expect to find in atmospheres of hot sub-Neptunes using the main loop of our pipeline Figure 1. For some selected cases we investigate how these predictions compare to a more detailed cloud model which we run with the cloud loop Figure 1. In these atmospheres we search for characteristic absorption features generated by pure and mixed cloud grains.

3.1 Expected condensates in hot atmospheres of sub-Neptunes

In this first part, we show which cloud species we can expect to find in the atmospheres of hot sub-Neptunes depending on their

composition. Note, that here we focus on the major condensates which could be stable in different types of atmospheres without studying them in detail and without incorporating a complex cloud model. We provide an overview of the condensates which can form in carbon (C)- oxygen (O)- nitrogen (N)-dominated and hydrogen (H)-dominated atmospheres. We also identify patterns in the temperature structures in the different atmospheric types.

Figure 3 shows an overview of the temperature-pressure structures of our grid of atmospheres. Each panel corresponds to twelve atmospheres for one atmospheric type with a certain C/O ratio. The rows show the three types from top to bottom: Type 1: O-, CO-, or C-dominated (depending on the C/O ratio), type 2: N-dominated and type 3: H-dominated. The columns indicate the C/O ratio of the atmosphere from left to right with C/O=0.1, C/O=0.5, C/O=1 and C/O=2. The temperature profiles are split into two categories. Blue temperature profiles correspond to atmospheres with low elemental sulphur and phosphorus abundance, X_S X_P 0.1 ppm and red temperature profiles show models with high elemental sulphur and phosphorus abundance of X_S X_P 1 %. This split illustrates the behaviour that sulphur and phosphorus rich atmospheres are hotter if the atmosphere is oxygen poor and hydrogen rich. PS can form in these cases and create an inversion in the atmosphere due to strong absorption in the UV and optical, see Figure 4. We focus on condensates which reach abundances of > 1 ppb. These are illustrated in Figure 5, which is organised in the same format as Figure 3. A choice of refractory abundances larger than solar could shift the results towards more stable condensate species and higher abundances. It is also to note that we don't take into account the altitude of formation and the extent of a condensate to determine its importance.

3.1.1 O-, CO-, and C-dominated atmospheres

In O-dominated atmospheres (C/O< 1) the near-surface region is the hottest part of the atmosphere because of the presence of greenhouse gases like H_2O and CO_2 . The temperature decreases with altitude reaching the lowest values of all our models with $T < 1000$ K at $P < 10^{-7}$ bar. This behaviour allows for a large variety of condensates to be stable. Due to the temperature structures being so similar for all the models in this atmospheric type, many of the condensates can be stable in multiple of these atmospheres. This is illustrated by Figure 5, where a large fractional occurrence is reached for multiple species in these atmospheres.

At C/O=0.1 we can expect the following condensates: $TiO_2(s, l)$, $SiO_2(s, l)$, $MgTi_2O_5(s, l)$, $MgSiO_3(s, l)$, $MgAl_2O_4(s, l)$, $Mg_3(PO_4)_2(s, l)$, $Mg_2TiO_4(s, l)$, $Fe_3O_4(s, l)$, $Fe_2O_3(s, l)$, $CaTiO_3(s)$, $CaSiO_3(s)$, $CaMgSi_2O_6(s)$, $Al_6Si_2O_3(s, l)$, $Al_2O_3(s, l)$ and $(P_2O_5)_2(s)$. Out of these species, $SiO_2(s, l)$, $TiO_2(s, l)$, $CaTiO_3(s)$ and $Fe_3O_4(s, l)$ are stable in all atmospheres of this type.

If the C/O ratio is increased to C/O=0.5, $(P_2O_5)_2(s)$, $Al_6Si_2O_3(s, l)$, $CaSiO_3(s)$ and $Fe_2O_3(s, l)$ do not form in our models anymore, but instead we find $Mg_2SiO_4(s, l)$, $Fe_2SiO_4(s)$, $FeO(s, l)$ and $MgTiO_3(s, l)$. Similarly to the case with C/O=0.1, $CaTiO_3(s)$, $SiO_2(s, l)$, and $TiO_2(s, l)$ are also stable in all models of this kind, in addition to $Fe_2SiO_4(s)$ and $MgAl_2O_4(s, l)$.

These differences show, that iron species are particularly sensitive to changes in the C/O ratio in O-atmospheres. At C/O=0.1 iron condenses mainly in its most oxidised forms $Fe_3O_4(s)$ and $Fe_2O_3(s)$. This changes as the C/O ratio is increased to 0.5 where major iron condensates are $Fe_2SiO_4(s)$ and $FeO(s, l)$. However, aluminium condensates and magnesium species are also affected since $Al_2O_3(s, l)$

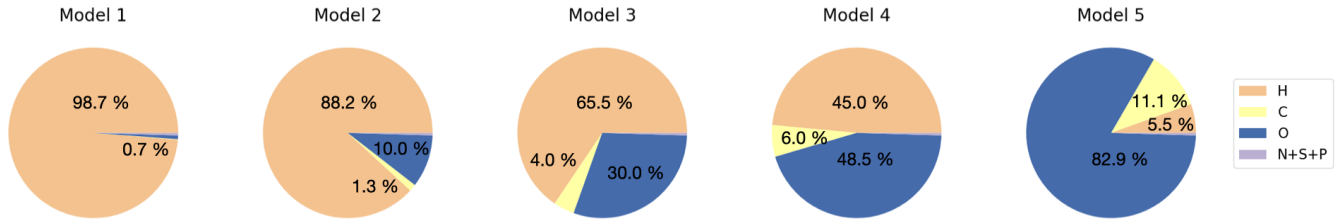


Figure 2. The pie charts show the percentage of the five volatiles in the atmosphere of the 55 Cnc e-type atmosphere and the four carbon- and oxygen- enriched cases. Orange represents the mole fraction of atomic hydrogen, blue the oxygen fraction and yellow shows the carbon fraction. In all five models, C/O 0.133 and the mole fractions of nitrogen, sulphur and phosphorus are kept constant with N 0.0008012, S 0.002597867 and P 0.0013388. Their sum is indicated in purple in the pie charts.

forms frequently in addition to $\text{MgAl}_2\text{O}_4(\text{s, l})$ at C/O=0.5 only and magnesium-oxides are overall less frequently found at C/O=1.

In CO-atmospheres (carbon and oxygen dominated atmospheres with (C/O=1), the temperatures reached at low pressures are much higher than in carbon poorer models. Only half of the CO-atmospheres reach temperatures $< 1250 \text{ K}$, whereas all models cool down below this threshold if C/O< 1. The gas phase of CO-atmospheres is dominated by the molecule CO, because carbon and oxygen have similar bulk abundances. Fewer solid and liquid species can be stable in fewer models compared to O-atmospheres, see Figure 5. The most common condensates in CO-atmospheres are $\text{Al}_2\text{O}_3(\text{s, l})$, $\text{CaTiO}_3(\text{s})$, and $\text{TiO}_2(\text{s, l})$ condensing in 75%, 60% and 60% of the models respectively. In addition, we find $\text{MgSiO}_3(\text{s, l})$, $\text{SiO}_2(\text{s, l})$, $\text{MgTi}_2\text{O}_5(\text{s, l})$, $\text{Mg}_2\text{SiO}_4(\text{s, l})$, $\text{Fe}(\text{s, l})$, $\text{Ti}_2\text{O}_3(\text{s, l})$ and $\text{TiN}(\text{s, l})$. In the four coldest atmospheres condensation sets on at altitudes between $5 \cdot 10^{-3} \text{ bar}$ and 10^{-4} bar . $\text{Al}_2\text{O}_3(\text{s, l})$, $\text{CaTiO}_3(\text{s})$ and $\text{TiO}_2(\text{s, l})$ are always the species condensing first. In the P+S poor CO-atmospheres with the highest H/O ratio as well as in the P+S rich CO-atmospheres with the lowest H/O ratio (the two turquoise and the dark red model), condensation can only happen between $10^{-4} - 10^{-7} \text{ bar}$. Mostly $\text{TiO}_2(\text{s, l})$, $\text{CaTiO}_3(\text{s})$ and $\text{Al}_2\text{O}_3(\text{s, l})$ condense in these regions. The medium and dark orange temperature profiles correspond to the atmospheres which are P+S poor, have a high H/O ratio and contain more nitrogen compared to hydrogen. This means that the bulk oxygen abundance in these cases is particularly low while nitrogen and carbon are abundant and the temperatures are low enough, resulting in the stability of very reducing species like $\text{TiC}(\text{s})$ and $\text{TiN}(\text{s})$. In the case which is P+S rich and hydrogen is the second most abundant volatile after carbon, the conditions are such that condensation cannot occur at all: The H/O ratio is high and PS can be stable, leading to temperatures which are high throughout the entire atmospheres.

C+O-dominated atmospheres with C/O=2 are C-dominated in their bulk composition. Despite these high total C/O ratio, the gas phase C/O often decrease to approximately unity. We will address this at the end of this section. Out of these models, the six compositions with low P+S abundance all show a decrease in temperature with altitude. The less carbon and oxygen and the more hydrogen, the hotter the atmosphere becomes at low pressures. The six C-dominated models rich in P+S have a temperature inversion and no condensation. The most reducing cases with more carbon and oxygen and less hydrogen (red models) cool with decreasing pressure above the inversion. Three condensation behaviours show depending on the temperature structures: both, oxides and carbides condense, only carbides condense or the atmosphere is purely gaseous. As shown in Figure 5, we find predominantly $\text{TiC}(\text{s})$, $\text{C}(\text{s})$ and $\text{Al}_2\text{O}_3(\text{s, l})$ in respectively 60%, 50% and 40% of our C-dominated models. Condensates can form between $1-10^{-2} \text{ bar}$ where there is a strong temperature drop. The four coldest models (blue) reach low enough temperatures for C

(s), $\text{Al}_2\text{O}_3(\text{s, l})$, $\text{MgO}(\text{s})$, $(\text{CaAl})_2\text{SiO}_7(\text{s})$, $\text{CaSiO}_3(\text{s})$, $\text{Ca}_2\text{SiO}_4(\text{s})$, $\text{SiO}(\text{s})$, $\text{Fe}(\text{s, l})$, $\text{Mg}_2\text{SiO}_4(\text{s, l})$ and $\text{MgSiO}_3(\text{s, l})$ to form. Two condensate layers of $\text{TiC}(\text{s})$ and $\text{C}(\text{s})$ can form in the two light turquoise models where the temperature drops to $1250 \text{ K} - 1300 \text{ K}$ at 10^{-8} bar , enhancing the occurrence rate of these two species in Figure 5 further.

We find that the C/O ratio of the gas phase in the C-atmospheres is only around 10% above unity. This is a consequence of heavy graphite rainout to the surface in these atmospheres. Hence, gaseous CO is the major carbon and oxygen carrier there. Temperature drops with altitude can lead to the stability of some oxygen bearing condensates in these atmospheres. At low enough temperatures and high enough pressures, oxygen can still be thermally stable in liquid and solid compounds even if the C/O ratio is close to unity. In certain cases, carbides and - in nitrogen-rich atmospheres - nitrides can rain out at low altitudes. This decreases the C/O ratio further with increasing altitude.

3.1.2 N-dominated atmospheres

In N-dominated atmospheres, there is a bifurcation in the temperature structures at each C/O ratio, see Figure 3. If C/O=0.1 or C/O=0.5, temperature profiles of oxygen poorer atmospheres with high H/O ratio (turquoise and orange models) are inverted. TiO can create these inversions around 10^{-4} bar (turquoise models). If PS forms as additional heating agent (orange models) it can lower the altitude of the inversions to pressures $> 10^{-3} \text{ bar}$. In models with low H/O ratio (dark blue and red), sulphur and phosphorus mostly form PO_2 and SO_2 and titanium is mostly in the form of TiO_2 . Hence, the surfaces are hot and the atmospheres cool with altitude.

The only cases for which condensation is possible, are the atmospheres with low H/O. Thus solids and liquids form in fewer models compared to the O-dominated atmospheres, see Figure 5. At C/O< 1, the most common condensates appear in 60% of the N-atmospheres. $\text{TiO}_2(\text{s, l})$, $\text{SiO}_2(\text{s, l})$, $\text{MgTi}_2\text{O}_5(\text{s, l})$, $\text{MgAl}_2\text{O}_4(\text{s, l})$, $\text{Mg}_3(\text{PO}_4)_2(\text{s, l})$, $\text{Fe}_3\text{O}_4(\text{s, l})$, $\text{CaTiO}_3(\text{s})$, and $\text{Al}_2\text{O}_3(\text{s, l})$ form at both C/O=0.1 and C/O=0.5. Along those we find $\text{Mg}_2\text{TiO}_4(\text{s, l})$, $\text{CaMgSi}_2\text{O}_6(\text{s})$, $\text{Al}_6\text{Si}_2\text{O}_3(\text{s, l})$, and $(\text{P}_2\text{O}_5)_2(\text{s})$ at C/O=0.1, and $\text{Mg}_2\text{SiO}_4(\text{s, l})$, $\text{MgSiO}_3(\text{s, l})$, $\text{Fe}_2\text{SiO}_4(\text{s})$ and $\text{FeO}(\text{s, l})$ at C/O=0.5.

In N-dominated atmospheres with C/O=1, the thermal structures are majorly affected by the P+S content, rather than the H/O ratio. The red and orange models are hotter than the blue models and all have inversions between $0.1 - 10^{-3} \text{ bar}$. The P+S poor models (blue and turquoise) have non existing to small inversions at high pressures. The models with higher H/O ratios have inversions at low pressures created by atomic Fe. The only three cases where condensation can proceed are the dark blue models with low H/O ratio and low P+S

abundance. The two stable condensates forming there are $\text{TiN}(\text{s}, \text{l})$ and $\text{Al}_2\text{O}_3(\text{s}, \text{l})$.

N-dominated atmospheres with $\text{C}/\text{O}=2$ show three types of temperature structures: The atmospheres with low $\text{P}+\text{S}$ abundance and low H/O ratio show a strong decrease in temperature from 2300 K to 1000 K between 1 and 0.01 bar. $\text{P}+\text{S}$ poor models with high H/O cool down to 1400 – 1600 K, then continue isothermally up to 10^{-5} bar where they have a steep temperature inversion. All models rich in $\text{P}+\text{S}$ have a temperature inversion between 10^{-2} bar and 10^{-3} bar. These atmospheres are strongly heated by CN and PS . Figure 5 shows that the most common condensates in N-dominated atmospheres with $\text{C}/\text{O}=2$ are $\text{TiC}(\text{s}, \text{l})$ and $\text{C}(\text{s})$. Likewise to the C-dominated atmospheres we also find $\text{Al}_2\text{O}_3(\text{s}, \text{l})$, $\text{CaSiO}_3(\text{s})$, $\text{Mg}_2\text{SiO}_4(\text{s}, \text{l})$, $\text{Fe}(\text{s}, \text{l})$, $(\text{CaAl})_2\text{SiO}_7(\text{s})$, $\text{Ca}_2\text{SiO}_4(\text{s})$, $\text{MgO}(\text{s})$, and $\text{SiO}(\text{s})$. $\text{MgSiO}_3(\text{s}, \text{l})$ does not reach abundances > 1 ppb. Species which don't appear in C-dominated atmospheres but are stable here are $\text{CaS}(\text{s})$ and $\text{SiC}(\text{s})$, each appearing in 10% of the cases and $\text{AlN}(\text{s})$ condensing in 30% of the models. The condensation is strongly affected by the sulphur and phosphorus content. In none of the $\text{P}+\text{S}$ rich atmospheres (red and orange models) condensation can take place. In N-dominated atmospheres with $\text{C}/\text{O}=2$, low $\text{P}+\text{S}$ abundance and low H/O ratio (three darkest blue models), condensates form in the region of the temperature drop. In Figure 5, these species have lower occurrence in the N-type atmospheres compared to the C-atmospheres because only the three models with carbon and oxygen as major secondary volatiles in N-atmospheres are cold enough, whereas all $\text{P}+\text{S}$ poor models in the C-dominated atmospheres are cold enough for condensation. In $\text{P}+\text{S}$ poor models with high H/O ratio, $\text{SiC}(\text{s})$ and $\text{AlN}(\text{s})$ condense in the isothermal region between 0.1 – 10^{-5} bar.

3.1.3 H-dominated atmospheres

In H-dominated atmospheres, there is a similar bifurcation in the temperature structures as in N-dominated atmospheres. However, we find less stable condensates and we find them in fewer of the models compared to N-dominated atmospheres at all C/O ratios. At low pressures, the non inverted atmospheres cannot cool down as efficiently as in the N-dominated models because of increasingly reducing conditions favouring the formation of strong UV and optical absorbers. At low C/O ratios and high pressures, green house gas heating is more efficient in H-dominated atmospheres, because more H_2O forms compared to the N-dominated cases. At $\text{C}/\text{O}=0.1$ and $\text{C}/\text{O}=0.5$, a lot of oxygen is in O_2 in N-atmospheres. However in H-atmospheres, H_2O is abundant and as a green house gas it heats up the near surface layers, resulting in a hotter deep atmosphere in these types.

In terms of condensates, we find stable species $\text{TiO}_2(\text{s}, \text{l})$, $\text{SiO}_2(\text{s}, \text{l})$, $\text{MgTi}_2\text{O}_5(\text{s}, \text{l})$, $\text{MgSiO}_3(\text{s}, \text{l})$, $\text{MgAl}_2\text{O}_4(\text{s}, \text{l})$, $\text{Mg}_3(\text{PO}_4)_2(\text{s}, \text{l})$, $\text{CaTiO}_3(\text{s})$ and $\text{Al}_2\text{O}_3(\text{s}, \text{l})$. Additionally, $\text{CaMgSi}_2\text{O}_6(\text{s})$ and $\text{Mg}_2\text{SiO}_4(\text{s}, \text{l})$ form if $\text{C}/\text{O}=0.1$ and $\text{Ti}_4\text{O}_7(\text{s}, \text{l})$, $\text{Ca}_2\text{SiO}_4(\text{s})$, $(\text{CaAl})_2\text{SiO}_7(\text{s})$, and $\text{CaSiO}_3(\text{s})$ can be stable if $\text{C}/\text{O}=0.5$. The most common condensate in both sub-types is $\text{Al}_2\text{O}_3(\text{s}, \text{l})$ forming in 50% of the atmospheres with $\text{C}/\text{O}=0.1$ and in 40% of the atmospheres with $\text{C}/\text{O}=0.5$.

In H-dominated atmospheres with $\text{C}/\text{O}=1$, the temperature never drops below 1400 K between $10 - 10^{-8}$ bar, see Figure 3. Carbon and oxygen reside in the gas phase and no condensation can take place. It is to note, that this behaviour could potentially change in atmospheres with higher refractory abundances.

H-atmospheres with $\text{C}/\text{O}=2$, low $\text{P}+\text{S}$ abundance and low H/O ratio show a strong decrease of temperature from 2300 K to 1600 K between 1 – 0.01 bar. $\text{P}+\text{S}$ poor models with high H/O (turquoise

models) cool down to 1400-1600 K and are then isothermal up to 10^{-5} bar before a steep temperature inversion. In the upper atmosphere, CN creates the temperature inversion at $5 \cdot 10^{-6}$ bar. All the models with high $\text{P}+\text{S}$ content have a temperature inversion between 10^{-2} bar and 10^{-3} bar due to the presence of PS . Overall, three condensates are stable in H-atmospheres with $\text{C}/\text{O}=2$: $\text{C}(\text{s})$ and $\text{TiC}(\text{s})$ form in 50% of the atmospheres and $\text{SiC}(\text{s})$ forms in 25% of the atmospheres. Likewise to N-dominated atmospheres, the sulphur and phosphorus content affects the condensability of H-dominated atmospheres with high C/O ratio. In $\text{P}+\text{S}$ rich atmospheres nothing condenses. In atmospheres with low $\text{P}+\text{S}$ abundance which are rich in carbon and oxygen, $\text{TiC}(\text{s})$ can condense in the temperature drop between 1 – 0.01 bar. Graphite $\text{C}(\text{s})$ is stable throughout most of the atmosphere. In $\text{P}+\text{S}$ poor models which are also poor in carbon and oxygen, $\text{SiC}(\text{s})$ is stable in the isothermal region in addition to $\text{TiC}(\text{s})$ and $\text{C}(\text{s})$.

3.1.4 Summary

We have explored condensation in various atmospheric types which all have refractory abundances at solar values. Hence the conclusions we make are valid for these types only and might change with the inclusion of outgassing to our models. Atmospheres which cool down the furthest at low pressures are the phosphorus and sulphur poor models with the lowest H/O ratio (dark blue models and O-atmospheres). These are the cases in which we expect clouds to be the most stable, especially at high altitudes $P < 0.01$ bar. Depending on the atmospheric type, on the H/O ratio and on the C/O ratio, different solid and liquid species are stable. The H/O ratio is crucial in determining whether an inversion can occur. In atmospheres with $\text{C}/\text{O} < 1$, O-atmospheres are inversion free and the same holds for N-atmospheres if they have a high oxygen content. For the compositions we investigate, the switch between an inversion and no inversions in N-atmospheres with $\text{C}/\text{O} < 1$ happens on the order of $\text{H}/\text{O}=10$ for $\text{P}+\text{S}$ poor models and on the order of $\text{H}/\text{O}=1$ for $\text{P}+\text{S}$ rich models. For $\text{C}/\text{O} \geq 1$, the sulphur and phosphorus content are also important to consider. H-, C-, and N-atmospheres with high sulphur and phosphorus content have inversions even if their H/O ratio is low. In terms of condensate stability at low C/O ratio, we predominantly find $\text{CaTiO}_3(\text{s})$ and $\text{TiO}_2(\text{s}, \text{l})$ in N-atmospheres, $\text{CaTiO}_3(\text{s})$, $\text{TiO}_2(\text{s}, \text{l})$ and $\text{SiO}_2(\text{s}, \text{l})$ in O-atmospheres and $\text{CaTiO}_3(\text{s})$ and $\text{Al}_2\text{O}_3(\text{s}, \text{l})$ in H-atmospheres. Literature on the stability of condensates in atmospheres of Hot Jupiters (H-atmospheres) by [e.g.] Wakeford et al. (2017) is in agreement with these findings. At high C/O ratio, liquid and solid oxides form only in specific cases where the bulk oxygen abundance is high enough and where the temperatures are low. These conditions can either be provoked by rainout of graphite or an initially large bulk oxygen abundance. Low sulphur and phosphorus abundances tend to result in lower temperature conditions compared to sulphur and phosphorus rich atmospheres because the heating agent PS does not form in the former. Nitrides and carbides can be stable in the oxygen poorest atmospheres, i.e. where the H/O ratio and the C/O ratio are high.

3.2 Stability of condensates: The role of the oxygen budget

In this section, we explore in more detail the impact of the oxygen abundance of the atmosphere on condensate formation. The volatile abundances of the five compositions we consider for this study are the compositions described in section 2.6 and illustrated in form of pie charts in Figure 2. Figure 6 shows the atmospheric

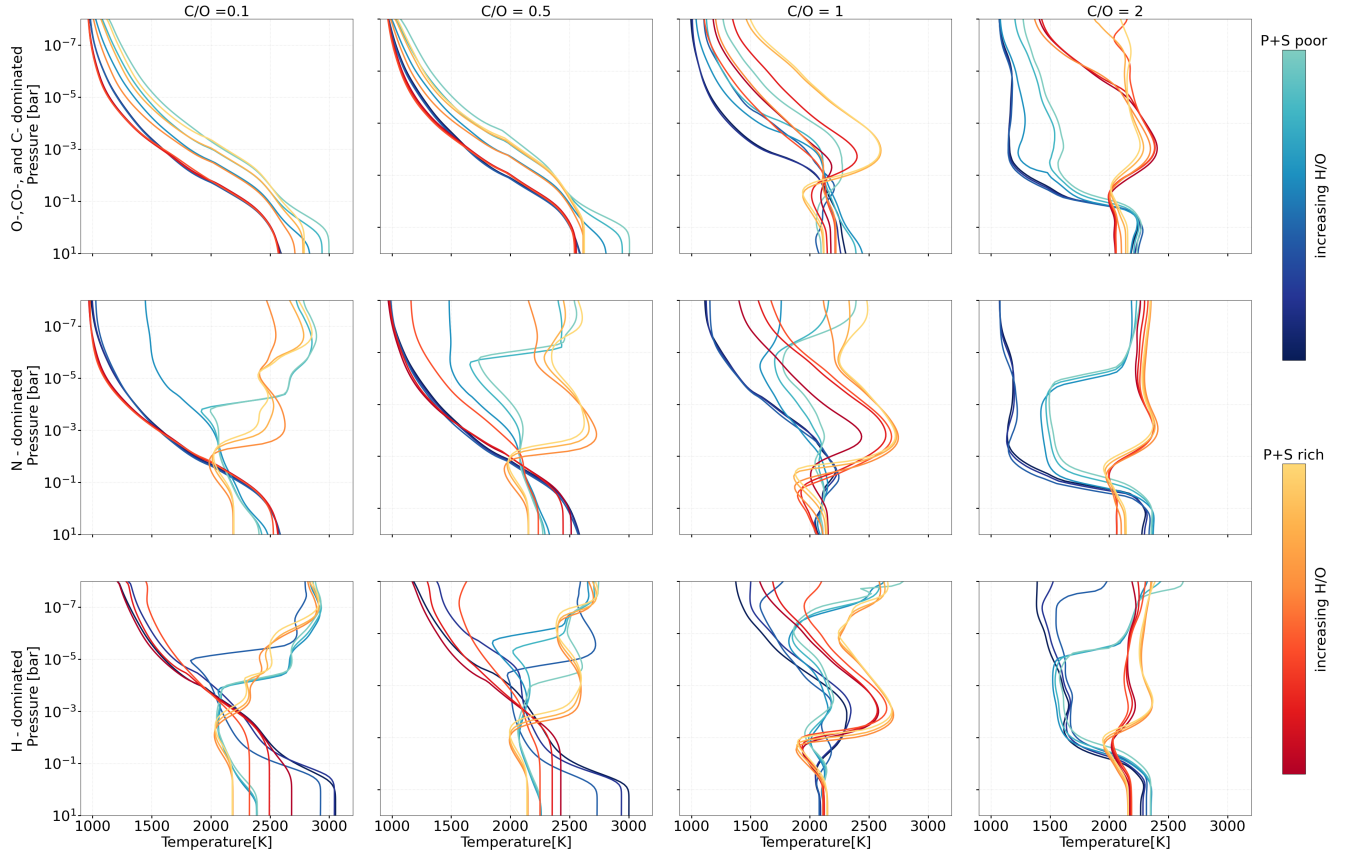


Figure 3. Temperature structures of all models from our grid study. They are grouped according to their atmospheric type. The row indicates the dominating volatile in the atmosphere and the column indicates the C/O ratio of the model. The six blue and turquoise profiles correspond to models which have low P+S abundance. The six red and orange profiles have high P+S abundance. In each of these groups, the shade of the colour indicates the H/O ratio. The darker the blue/red shade, the lower the H/O ratio, the greener/yellower, the higher the H/O ratio. It is to note, that these colours do not indicate a numerical value of H/O ratio. The colour bar merely indicates a trend, but the lowest H/O ratio for H-atmospheres is higher than the lowest H/O ratio for O-atmospheres.

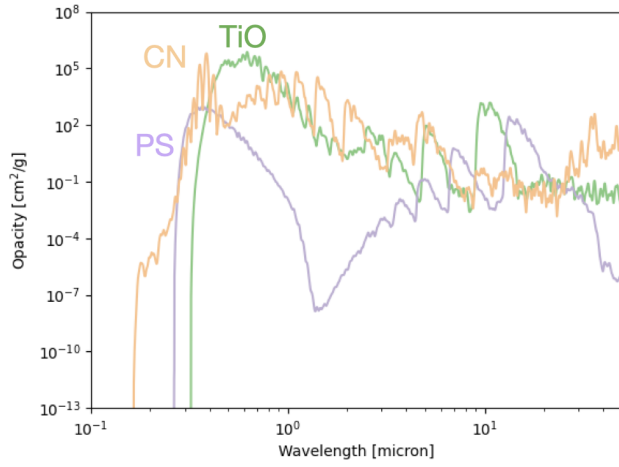


Figure 4. Opacities of some relevant strongly UV and optical absorbing species at 2000 K and 10^{-5} bar. The altitude is chosen according to where the opacity contribution is the strongest.

gas-phase compositions, temperature-pressure profiles, and resulting condensates for this set of models. The oxygen abundance increases from left to right across the five models. The atmospheric composition transitions from a H_2 -dominated atmosphere with $\text{O/H}=0.0072$

(model 1), to a $\text{H}_2/\text{H}_2\text{O}$ mixture with $\text{O/H}=0.011$ (model 2), then to a H_2O -dominated atmosphere with $\text{O/H}=0.46$ (model 3), followed by a $\text{H}_2\text{O}/\text{CO}_2$ atmosphere with $\text{O/H}=0.93$ (model 4), and finally to an O_2/CO_2 -dominated atmosphere with $\text{O/H}=15$ (model 5). The amount of available oxygen affects the type of condensates that can form in two ways:

Thermal Structure: The O/H ratio and the C/O ratio have a strong influence on the thermal structure of the atmosphere (see section 3.1): At extremely high O/H ratios and low C/O ratio - dark blue and red models in the two first columns of Figure 3- , we expect high surface temperatures and then a decrease of temperature with altitude which reaches temperatures < 1300 K between $10^{-5} - 10^{-8}$ bar. This favours cloud formation in those regions. At a lower H/O ratio, major optical absorbers (e.g. TiO, CN and PS) can form depending on the composition and heat up the atmosphere, creating inversions and preventing cloud formation.

Condensate Formation: Higher oxygen abundances promote the formation of a greater number of condensates. As shown in Figure 5, the most common condensates are oxides. In chemical equilibrium, the formation of condensates is governed by the thermal stability of all gaseous, liquid, and solid species and the species which are the most stable will condense first. Nothing condenses in the atmosphere of model 1, which is dominated by molecular hydrogen see Figure 6. However, part of the atmosphere rains out to the surface in the form of $\text{CaTiO}_3(\text{s})$, $\text{Al}_2\text{O}_3(\text{s})$ and $\text{Ti}_3\text{O}_5(\text{s})$. The inversion is



Figure 5. Shown are all condensates which appear in at least one model in the full grid and reach volume mixing ratios in the atmosphere ≥ 1 ppb. Each panel represents one out of twelve atmospheric types: The row indicates the dominating volatile in the atmosphere and the column indicates the C/O ratio of the model. Each panel displays condensates as coloured bars, where each condensate has its own attributed colour and the name is indicated in the bar. The x-axis shows the fraction of models in which each condensate appears for the corresponding atmospheric type.

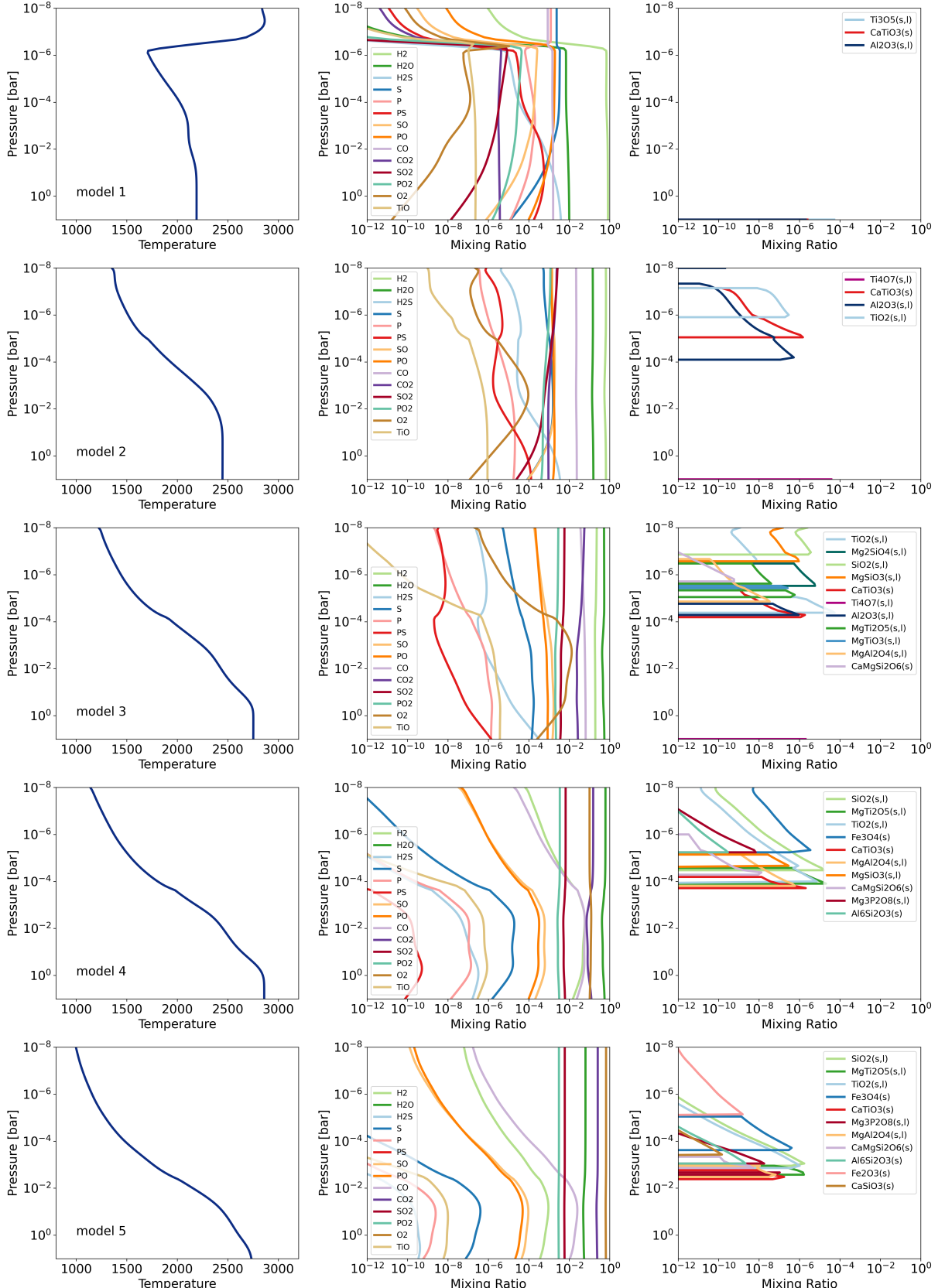


Figure 6. Temperature profiles (left hand side column), relevant gas phase species (middle column) and condensates (right hand side column) of the five cases shown in Figure 2. The oxygen abundance is increased from top to bottom of the figure. In all cases, refractory elements are assumed to have solar abundances. The Figure highlights the cooling of the atmosphere and the increase in condensed species abundances with an increase in oxygen abundance.

caused by strong short-wave absorbers, mainly PS, which can form in this extremely reducing environment. This is similar to the P+S rich cases of H-dominated atmospheres discussed in section 3.1. In an atmosphere with a slightly higher oxygen budget - model 2, H₂ is still the major gas phase component. Phosphorus and sulphur form PO, SO, SO₂ and PO₂, S and P instead of PO, SO, S, P, HS and PS like in model 1. Hence, the temperature inversion has disappeared from one model to the other. This allows the most thermally stable condensates to form. As shown in Figure 6, these are in order at which they form from bottom to top of the atmosphere: Al₂O₃(s), CaTiO₃(s) and TiO₂(s, l). Ti₄O₇(s) is also thermally stable under the given conditions, but it rains out at the planetary surface. These particularly stable species are also the ones which can form in most of the compositions we explore in our grid in section 3.1. As the oxygen budget of the atmosphere is increased to O/H=0.46 in model 3, CaTiO₃(s) and Al₂O₃(s) remain the dominating candidates forming at the highest temperatures. At slightly colder temperatures, Mg-oxides such as Mg₂SiO₄(s, l) and MgTi₂O₅(s, l) form, followed by SiO₂(s, l), MgSiO₃(s, l) and TiO₂(s, l). Iron only condenses in oxidised form when the temperatures are low and the oxygen budget is high. A fraction of O/H=0.46 in models 3 is not enough for stable iron oxides, but with O/H=0.93 in model 4, Fe₃O₄(s, l) becomes stable at pressures < 10⁻⁵ bar. In model 5, Fe₃O₄(s, l) is stable between pressures of 10^{-3.5} to > 10⁻⁵ bar, where it is replaced by its more oxidised version Fe₂O₃(s, l). This behaviour can be traced back to the dependence of the stability of solid and liquid oxides on oxygen abundance as well as on pressure and temperature conditions. Seidler et al. (2025) investigate this behaviour for a range of condensates. They find that silicates and magnesium- oxides can condense first at mediate oxygen fugacities. Similarly to what our models predict, they also conclude that the iron condensates Fe₃O₄(s) and the more oxidised form Fe₂O₃(s) only form at particularly high oxygen fugacities.

One factor which can raise the condensation temperature is enhancement of the abundance of the related vapour species to form certain condensates. Similarly to how an increased oxygen abundance can favour the condensation of oxides. If the condensing species' abundance is raised, the condensation curve can move towards higher temperatures, and vice versa if its abundance decreases. This means, that in general, the condensation temperature of refractory rich clouds is higher for metal rich atmospheres than for metal poor cases.

3.3 A more complex cloud model reveals thicker clouds

To explore how different cloud formation models affect the results, we compare the composition and vertical extent of clouds using the dynamical cloud model ExoLYN and contrast these with our previous chemical equilibrium calculations using rainout. We use the O₂/CO₂ atmosphere (model 5) for this comparison, as it produces the largest amount of condensates. We also explore a carbon rich scenario using model 5 as a baseline and enhancing the C/O ratio. To highlight the differences of two extremes we choose a high eddy diffusion coefficient of $K_{zz} = 10^{10} \text{ cm}^2 \text{s}^{-1}$ in the cloud formation model for our comparison. We then investigate in greater depth the effect of vertical mixing on cloud extent and particle size in a separate section. We include cloud species and their condensation reactions as listed in Table 3.

3.3.1 Clouds in O-dominated atmospheres

Figure 7 shows how the cloud in model 5 predicted with ExoLYN compares to the rainout scenario. With both approaches, maximal

cloud masses > 10 ppm are reached. One difference between the two cases is the extent of the cloud. The mass of the cloud in the rainout model is concentrated at the bottom layers. It decreases drastically with altitude above 10⁻⁴ bar. The bottom cloud layer, below which material starts to evaporate is situated around 0.01 bar. The cloud in the dynamical model reaches mass mixing ratios higher than 10 ppm between 10⁻² – 10^{-6.5} bar and stretches to 10^{-7.5} bar. The bottom of the cloud is located at pressures > 0.01 bar. The most stable solid species in the rainout model, evaporating at the hottest temperatures is CaTiO₃(s). MgTi₂O₅(s, l) is stable around 10⁻² bar with a mass mixing ratio of 5 – 10 ppm depending on the altitude. It is replaced by 0.1 ppm Mg₃(PO₄)₂(s, l) and 5 ppm TiO₂(s, l) and SiO₂(s, l) above 10⁻² bar. In the dynamical model, Mg₂TiO₄(s) is most abundant at the cloud bottom, where it reaches mass mixing ratios > 1 ppm. At ≈ 0.05 bar, TiO₂(s) condensation becomes stable making the latter the major cloud forming material with MgTi₂O₅(s) as the second most abundant species. Two factors enhance the MgTi₂O₅(s) extent in the dynamical model compared to the equilibrium model:

Mass conservation in the rainout approach: In the rainout approach, the atmospheric mass is not conserved in the layers above the condensate because all condensed elements are removed from the atmosphere when they rain out. In this case, MgTi₂O₅(s) raining out results in a change of composition above each layer where MgTi₂O₅(s) is stable. With decreasing pressure, the temperature also decreases and additional species such as TiO₂(s, l) and Mg₃(PO₄)₂(s, l) become stable, replacing MgTi₂O₅(s). In reality, the material between the different atmospheric layers would be mixed, and all of these species would condense at the same time.

Non-equilibrium processes in the dynamical model: A combination of the different dynamical cloud formation processes leads to abundances deviating from chemical equilibrium. In ExoLYN, sedimentation and vertical mixing are competitive processes affecting the cloud particle size and the cloud extent. Particles which form at lower altitudes can be transported to higher atmospheric layers. Therefore, MgTi₂O₅(s) can stay stable throughout the upper layers of the atmosphere, if the conversion from MgTi₂O₅(s) to TiO₂(s) happens very slowly. In addition to this time dependence of the mechanisms, nucleation can also promote formation of solid and liquid species in regimes where equilibrium alone does not allow condensation. The reason for this is that the presence of condensation nuclei provides a surface onto which material can condense and accumulate in solid or liquid form. Additional magnesium bearing species can form in the dynamical model. Almost 1 ppm of the cloud mass is locked into MgSiO₃(s) and Mg₂SiO₄(s) even though both of them are not abundant in chemical equilibrium. TiO₂(s) is the dominating cloud component in the dynamical cloud model throughout most of the cloud, with mass mixing ratios ≈ 50 ppm. At pressures ≤ 10^{-2.5} bar, FeO(s) and MgTi₂O₅(s) are the second most abundant cloud components after TiO₂(s) and reach mass mixing ratios of ≈ 5 ppm. In the rainout model, iron condenses mainly as Fe₂O₃(s) and Fe₃O₄(s) at pressures smaller than 5 · 10⁻² bar. In the dynamical model, these two species are abundant in this pressure range as well with mass mixing ratios of ≈ 0.5 – 1 ppm, where we also find Fe₂SiO₄(s) with an abundance of ≈ 0.5 ppm. In both models, SiO₂(s) is the major silicon reservoir of the cloud grains.

The comparison between the two models shows that the choice of the model matters. The mass of the predicted cloud, its extent, and its composition depend on this choice. Because material is taken out of the atmosphere in every layer with rainout, the available material for condensation is limited and decreases with increasing altitude. As a result, the rainout model underestimates the extent and the mass of the cloud. In addition, the predicted cloud composition can also

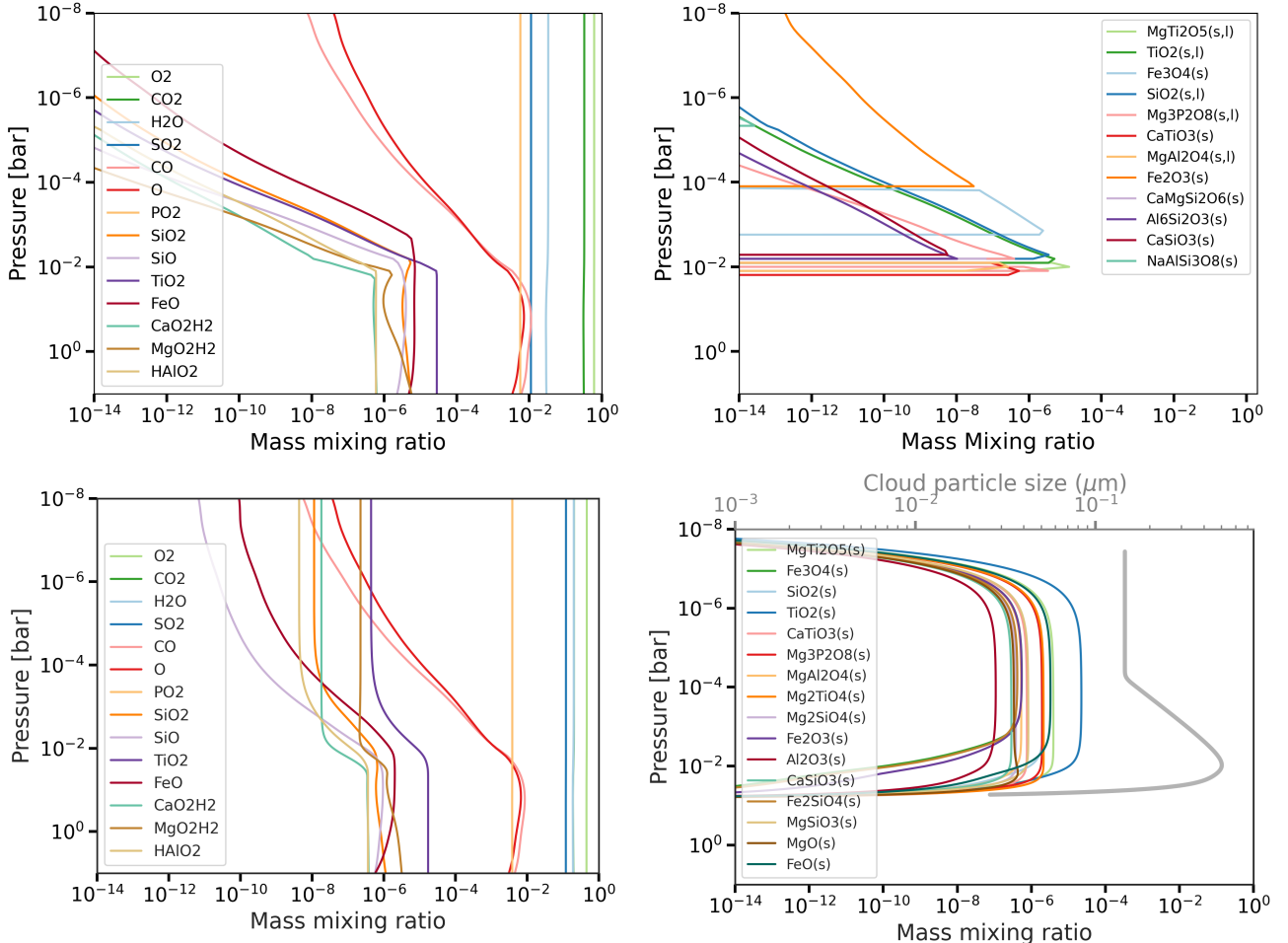


Figure 7. Mass mixing ratios and condensate/cloud of the O_2/CO_2 atmosphere - model 5. The 15 major gas phase species are shown in the left hand side column and the solid and liquid species in the right hand side column. The upper row shows the chemistry computed with the rainout approach with FASTCHEM3. For comparative purposes to ExoLyn we have converted the standardised output of volume mixing ratios to mass mixing ratios. In the bottom row, we have computed the cloud mass mixing ratios, particle sizes and the gas phase with the cloud formation model ExoLyn and FASTCHEM3 combined as described in section 3.3. The grey curve in the cloud panel indicates the particle size, and the coloured lines represent the mass mixing ratios of the individual cloud components.

be inaccurate because the species which are only thermodynamically stable deep in the atmosphere cannot be transported upwards. The dynamical cloud model can present a more accurate estimate of the cloud mass, extent, and composition but requires knowledge of the nucleation rate and mixing strength in the planetary atmosphere. Equilibrium chemistry alone does not provide cloud particle sizes, however the cloud model does. These are important to predict the extent of the cloud, since larger particles settle more efficiently than small particles. In our cloud model with vertical transport of $K_{zz} = 10^{10} \text{ cm}^2 \text{s}^{-1}$, the particle sizes range between $0.1 - 0.2 \mu\text{m}$, with larger particles at greater depths because settling is the strongest there. Different particle sizes also lead to different spectral features, since the particle size determines which wavelengths get scattered the strongest. We will discuss spectral features in section 3.4. One source of uncertainty for the grain composition in the dynamical cloud model which could also explain some of the discrepancies between the two approaches is the fact that the distribution of elements in the mixed cloud is influenced by the reaction pathways we take into account with ExoLyn.

3.3.2 Clouds in C-dominated atmospheres

The reaction pathways for clouds in carbon rich environments are poorly studied. We select the reaction pathways for $TiC(s)$, $SiC(s)$ and $C(s)$ from proposed reactions by Helling et al. (2017) according to which pathways result in the largest cloud mass. In sections 3.1 and 3.2 we have demonstrated that the cloud composition and extent are both affected by the C/O ratio, the abundance of volatiles and the temperature and pressure. In this section we investigate how a higher C/O ratio could affect the atmosphere and the clouds. We construct for this purpose a C-atmosphere by taking the example case of Figure 2 model 5 discussed in section 3.3.1. We keep the HNPS abundances but set the C/O ratio to $C/O=2$. Figure 8 shows temperature structure, gas composition and cloud composition of this atmosphere.

The gas composition is drastically different from the O_2/CO_2 -atmosphere. The major gaseous component is CO reaching almost a mixing ratio of unity. Part of the graphite has rained out to the surface. Nevertheless a thick graphite cloud still extends from the near surface region to the upper most layers of the atmosphere. Mixed into the graphite grains are $Al_2O_3(s)$, $Fe(s)$ and $TiC(s)$. The cloud forms a two layer structure, because of the shape of the temperature profile. The grain sizes are particularly large in the lower layer in the near surface

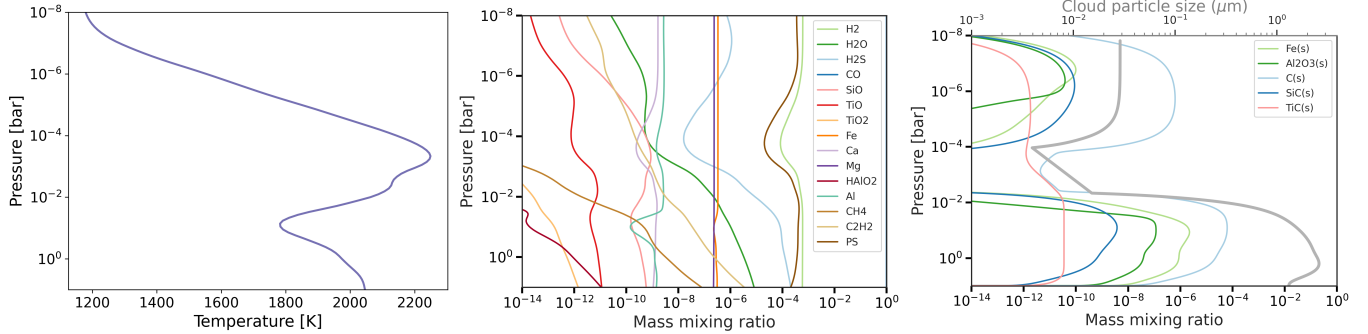


Figure 8. C-atmosphere which is like model 5 but with C/O=2. Shown are temperature structures in the first column, 15 of the important mass mixing ratios of the gas phase in the second column and mass mixing ratios of the cloud components in the third column. We have computed the cloud mass mixing ratios, particle sizes and the gas phase with the cloud formation model ExoLYN and FASTCHEM3 combined as described in section 3.3. The grey curve in the cloud panel indicates the particle size, and the coloured lines represent the mass mixing ratios of the individual cloud components. The reaction rates we used are listed in Table 3.

regions, reaching diameters $> 1 \mu\text{m}$ between $10 - 0.01$ bar. This lower layer ends above 0.01 bar with the first temperature inversion. A second layer reappears around 10^{-4} bar, where the atmosphere has cooled down again. Overall, the thick carbon cloud deck dominated by graphite agrees with our finding in the grid study section 3.1, that graphite clouds are a particularly stable cloud species in C-dominated atmospheres.

3.4 Spectral features of highly refractory clouds

3.4.1 Optical properties of dust grains

In this section we identify the potential features of all dust particles which appear in our grid Figure 5 and for which optical data is available. We use these features to analyse our spectra in section 3.4.2 and section 3.4.3 and to provide a comparison between spectral features of individual dust species and mixed cloud grains. In Figure 9 we show the extinction coefficients for the most common condensates in our model, computed as described in section 2.5. We show both amorphous and crystalline compounds if both are available (e.g. for SiO₂(s) and MgSiO₃(s)), because the structure of solid or liquid which the different materials can take is highly uncertain (e.g. Moran et al. 2024). Wakeford & Sing (2015) show extinction coefficients for some of the cloud species considered in this paper and conclude that the individual species will be difficult to discern, but they can be grouped according to their features and these groups can be identified. We also group the extinction coefficients according to the vibrational bands of the solids. As shown in Figure 9, some optical data is missing. There is a lack in refractive index data at wavelengths shorter than $0.4 \mu\text{m}$ for crystalline Fe₂SiO₄(s) and for MgAl₂O₄(s). For crystalline SiO₂(s) data is missing up to $5 \mu\text{m}$, for crystalline MgSiO₃(s) up to $1.1 \mu\text{m}$ and for amorphous MgSiO₃(s) and Mg₂SiO₄(s) as well as for Al₂O₃(s), refractive indices are available for wavelengths larger than $0.2 \mu\text{m}$ only.

The features of the small grains can be split into two categories: The UV and optical features (slope) and the features in the infrared. The species which could be identifiable from infrared features are SiO₂(s), SiO(s), Fe₂SiO₄(s), CaTiO₃(s), TiO₂(s), Al₂O₃(s), MgAl₂O₄(s), MgO(s), Fe₂O₃(s), Fe₃O₄(s), MgSiO₃(s), Mg₂SiO₄(s) and MgO(s). SiC(s), C(s) and TiC(s), Fe(s), FeS(s) and FeO(s) have a slightly less characteristic behaviour in the infrared part of their extinction coefficients. Distinct features in the optical and UV can arise from TiO₂(s), CaTiO₃(s), SiO₂(s), Fe₂O₃(s), MgO(s), SiC(s) and potentially other species for which we are miss-

ing UV data. The other materials for which we have data would mainly have a flattening effect on the spectrum and change the slope in the UV and optical compared to a purely gaseous atmosphere.

3.4.2 Spectral imprints of clouds in an O₂/CO₂ atmosphere

As discussed in section 3.1, O-dominated atmospheres are unlikely to have temperature inversions and are therefore favourable environments for high altitude cloud formation. In the following, we investigate whether clouds could be observable in O-dominated atmospheres of small planets. For all silicates we have used the amorphous properties to compute cloud opacities, since these are the most complete ones in wavelength space. However, we note that the features from crystalline structures could potentially be more distinct than those of their amorphous counterparts. In addition, experiments suggest a crystalline rather than an amorphous structure at high temperatures $T > 800$ K (Zeidler et al. 2013; Henning & Mutschke 1997; Kitzmann & Heng 2018). For our purposes, it is still a good enough approximation to take the amorphous properties due to the lack in crystalline data and due to the multiple structures which the crystal lattices can take depending on the exact atmospheric conditions (temperature, pressure and composition) (Moran et al. 2024). In addition, Moran et al. (2024) highlight, that is also unknown under which exact condition, liquid SiO₂(l) drops could form, resulting in "glassy", amorphous like features. Investigating the effects of different lattice structures on observability is beyond the scope of this paper.

Figure 10 shows the transmission spectrum resulting from model 5, the most oxidised of the five cases discussed in section 3.2. The orange model shows the cloudy spectrum with the mixed grain cloud model and the blue curve is the transmission spectrum without any clouds. Both are generated with petitRADTRANS as described in section 2.4. First, it is to note, that the atmospheric scale height of this atmosphere is small, with a mean molecular weight of $\mu = 34$. The features are almost non-existent, on the order of 5 ppm in the JWST MIRI wavelength range. Beyond $1 \mu\text{m}$, the cloudy and clear spectra are identical. The infrared is completely dominated by CO₂, CO, H₂O and SO₂ absorption. Since the cloud grain is primarily composed of TiO₂(s) mixed with FeO(s) and SiO₂(s), one could expect to see some of the characteristic infrared features from Figure 9 in the spectrum. However, none of them are visible. The reason for this are first of all the high abundances of CO₂, CO, H₂O and SO₂ in this particular atmosphere, leading to very strong opacities of these species in the infrared, see the mass mixing ratios in Figure 7.

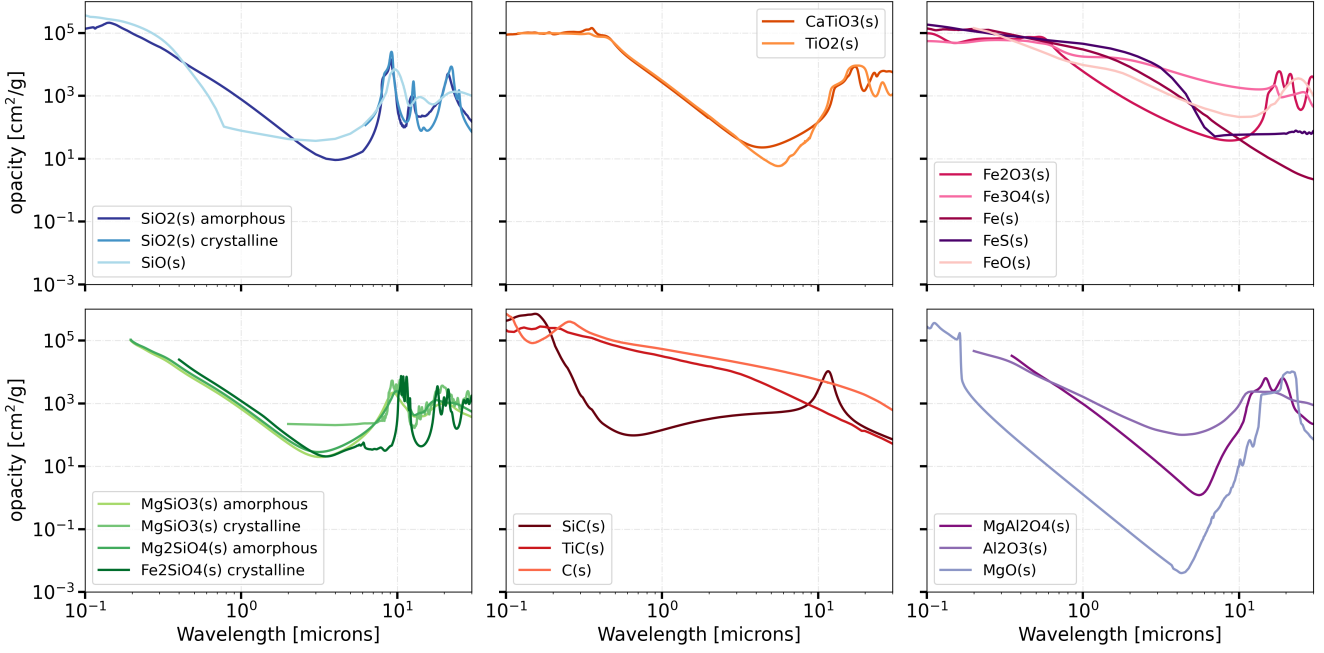


Figure 9. Extinction coefficient of solids as calculated with `OPTOOL` for a $0.01\text{ }\mu\text{m}$ large particle. We show all species in our models for which we could find refractive index data. The species are grouped according to their spectral features. For the species with a graph not spanning the full wavelength range between $0.1 - 30\text{ }\mu\text{m}$, part of the optical and UV data is missing. All the sources we use for the optical data here are listed in Table 4.

On the other hand, the cloud opacities in the infrared are in general weaker compared to the UV and optical. This is shown in Figure 9, where for a $0.01\text{ }\mu\text{m}$ large particle the extinction coefficient drops with wavelength. The Ti-O band has a unique refractive index drop in the UV between $0.2 - 0.5\text{ }\mu\text{m}$ which can lead to features in the UV and optical slope. However, in this atmosphere, this feature does not show either. The major effect of the clouds in the UV and optical is to dampen the features from gas species such as CO, O₂ and OH between $0.1 - 1\text{ }\mu\text{m}$.

The slope of the spectrum in the UV and optical could potentially be an indicator of the cloud species. However, it is strongly affected by the mean molecular weight of the atmosphere, the cloud species and their particle sizes (Pinhas & Madhusudhan 2017; Wakeford et al. 2017). These atmospheric properties need to be disentangled first before concluding on one particular cloud species from those spectral properties. Hence, one would need to look at infrared features to distinguish titanium oxides from each other and from other cloud species. However, as discussed this is not possible for this particular case, due to the infrared features being masked by features of gaseous species as well them being affected by the weakening of extinction properties of clouds with wavelength.

In general, the two spectra show that in such an atmosphere the mean molecular weight is extremely high and features from the gas phase and from the clouds are weak. It is to note that even though the cloud in the O₂/CO₂ atmosphere extends through six orders of magnitude in pressure, it does not flatten any spectral features in the infrared. In emission, the clouds have no features at all, see Figure 11. These results are likely impacted by our modelling choice. We are not accounting for the effect of clouds on the temperature structure, which is an essential component for the emission. Furthermore, we are using the same temperature-pressure profile for the emission and the transmission spectrum with a heat redistribution factor $f = \frac{1}{3}$. In reality, we would expect the terminators to be colder and the sub-

stellar point to be hotter, enhancing cloud formation in the regions probed by transmission.

3.4.3 Spectral imprints of clouds in a C- atmosphere

In the transmission spectrum of the C-atmosphere, spectral features mainly originate from CO, PS and some CO₂, COS and H₂S. The graphite cloud does not generate characteristic features but has a strong flattening effect on the gaseous features. This is due to the high and featureless extinction coefficient of graphite, see Figure 9. Even though C/O ratios of the gas phase can be similar for C-atmospheres with bulk C/O > 1 and CO-atmospheres with bulk C/O ≈ 1, flat spectral features can point towards high bulk C/O and to the formation of graphite clouds.

Graphite condensing on top of the silicate mantle has been suggested before by Kuchner & Seager (2005). The authors predict that such a carbon rich planet could point towards planet formation having taken place in locally carbon enriched environments of the disk. Hence detecting graphite clouds could provide us with some hints towards understanding disk dynamics and formation theory.

3.5 The effect of vertical mixing on cloud extent and composition

Vertical mixing is highly unknown, especially for hot, rocky planets. It is commonly parameterised by the eddy diffusion parameter K_{zz}. In gas giants, K_{zz} can span values between K_{zz} = $10^3\text{ cm}^2\text{ s}^{-1}$ to K_{zz} = $10^{12}\text{ cm}^2\text{ s}^{-1}$ (Venot et al. 2018). So far, we have been using a value of K_{zz} = $10^{10}\text{ cm}^2\text{ s}^{-1}$ in all of our models to investigate cloud formation with efficient gas replenishment. In this section, we explore the relevance that this parameter might have in the determination of the clouds by comparing our results with this strong eddy diffusion

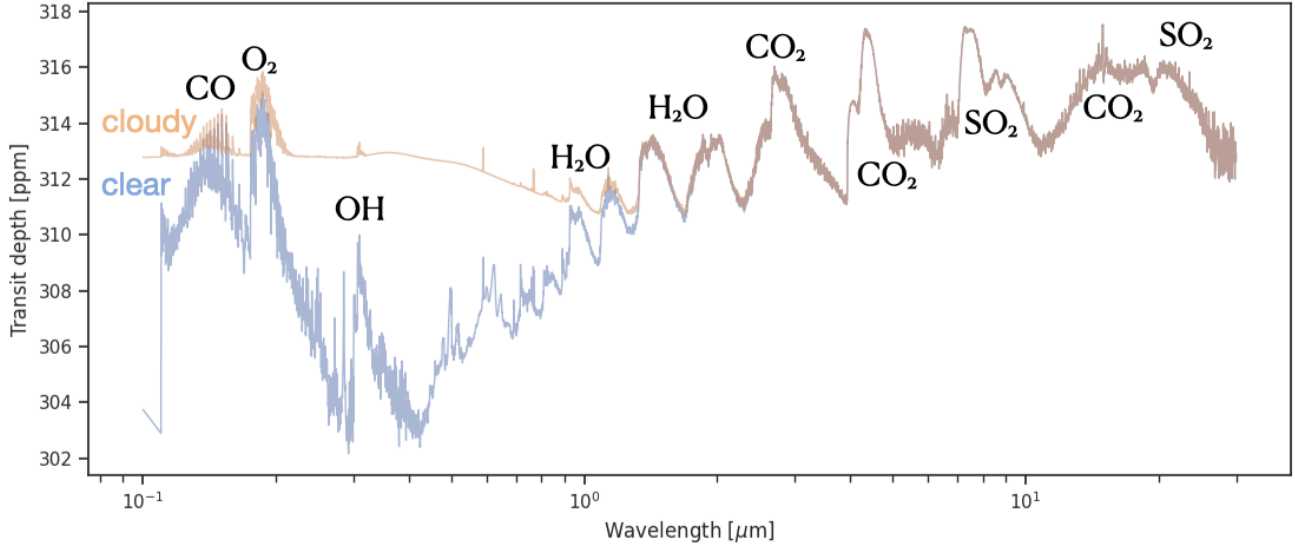


Figure 10. Transmission spectrum of the O_2/CO_2 atmosphere, model 5. Shown are features between $0.1 - 30\mu m$. The blue spectrum is the outcome if cloud opacities are omitted. The orange curve shows the full spectrum with clouds. Particularly the UV and optical are affected by cloud opacities. Major gas contributors to the spectrum are CO_2 , H_2O , SO_2 , O_2 , CO and OH .

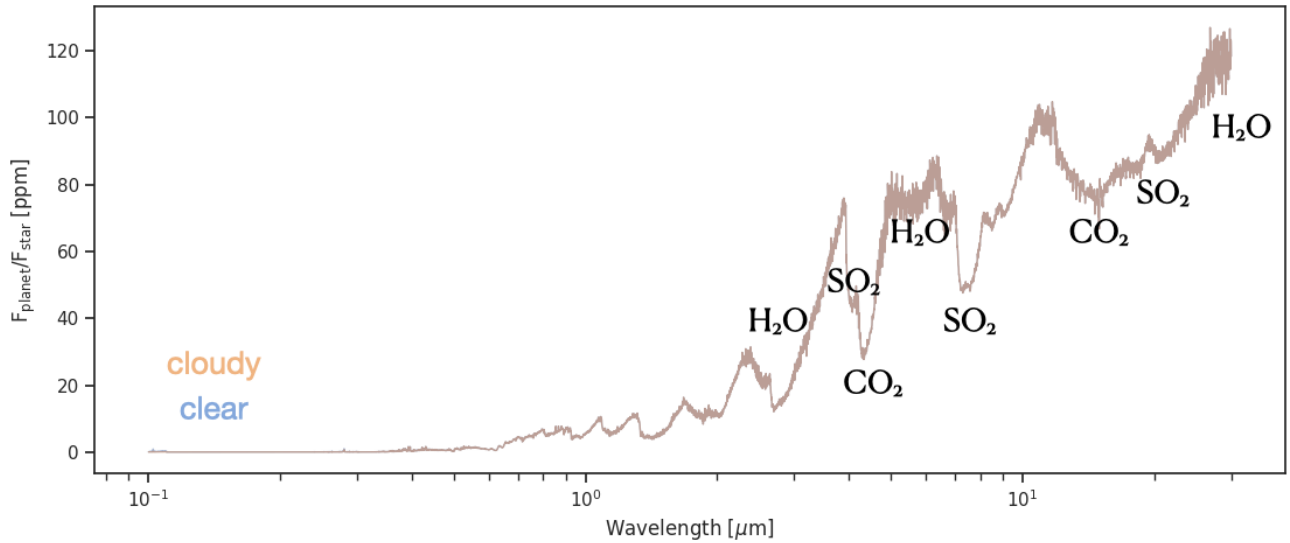


Figure 11. Emission spectrum of the O_2/CO_2 atmosphere, model 5. Shown are features between $0.1 - 30\mu m$. The blue spectrum is the outcome if cloud opacities are omitted. The orange curve shows the full spectrum with clouds. Major gas contributors to the spectrum are CO_2 , H_2O and SO_2 .

to the cases with weaker vertical mixing of $K_{zz} = 10^8\text{ cm}^2\text{s}^{-1}$ and $K_{zz} = 10^6\text{ cm}^2\text{s}^{-1}$.

Figure 13 shows the composition of the cloud in model 5 for different mixing strengths. As mixing decreases, the cloud becomes smaller in extent and less uniform. While for $K_{zz} = 10^{10}\text{ cm}^2\text{s}^{-1}$, the cloud extends from below 0.01 bar to $5 \cdot 10^{-8}$ bar, it evaporates at 10^{-6} bar if $K_{zz} = 10^8\text{ cm}^2\text{s}^{-1}$ and at 10^{-5} bar if $K_{zz} = 10^6\text{ cm}^2\text{s}^{-1}$. The composition and the particle sizes of the cloud grains also change with mixing strength. At the smallest mixing of $K_{zz} = 10^6\text{ cm}^2\text{s}^{-1}$, the layer structure of the cloud is particularly distinct. A bottom layer forms particles of $0.1\mu m$ between 0.05 bar - 10^{-2} bar. It is mainly composed of $Mg_2TiO_4(s)$, $TiO_2(s)$ and $Mg_3P_2O_8(s)$. Above this layer is a $TiO_2(s)$ cloud layer mixed with some $MgTi_2O_5(s)$ extending from

10^{-2} bar to $5 \cdot 10^{-3}$ bar with particles of sizes between $0.05\mu m$ to $0.1\mu m$. Above these pressures, iron oxides compose large fractions of the cloud. $FeO(s)$ condenses first followed by $Fe_3O_4(s)$. From $3 \cdot 10^{-5}$ bar on, the cloud is composed of primarily $FeO(s)$, $TiO_2(s)$ and $Fe_3O_4(s)$ with small particles $< 0.02\mu m$. This three layer structure is a similar structure to the one in the rainout model. It forms at weak mixing only because an inefficient transport of material means that solid species stay in the regions where they are thermodynamically stable. The particle size is largest towards the bottom of the cloud, where settling is the strongest. The cloud becomes thinner with altitude and the particles shrink. Overall, the species which condenses the most efficiently onto the cloud grains is $TiO_2(s)$. Settling of $CaTiO_3(s)$ and $Mg_2TiO_4(s)$ in the lower cloud layer is also

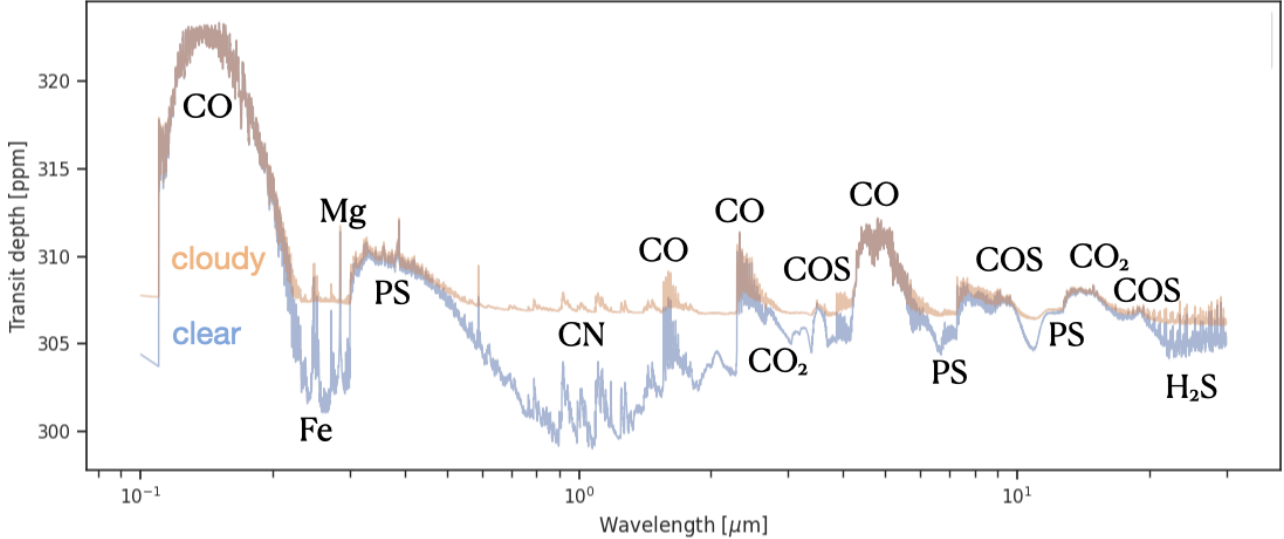


Figure 12. Transmission spectrum of the C-atmosphere, model 5 with $\text{C}/\text{O}=2$. Shown are features between $0.1 - 30 \mu\text{m}$. The blue spectrum is the spectrum if cloud opacities are omitted. The orange spectrum shows the full spectrum with clouds. The spectrum is strongly affected by graphite clouds through the entire wavelength range with a flattening effect.

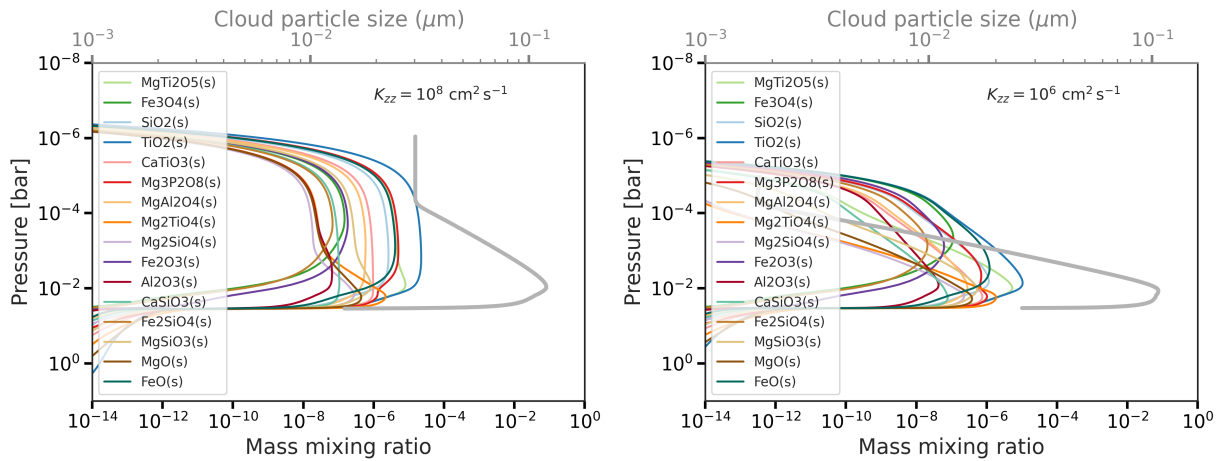


Figure 13. Shown are mass mixing ratios of the condensate/cloud mass mixing ratios in the atmosphere of model 5. We have computed them with ExoLyn and FASTCHEM3 combined as described in section 3.3. The left hand side panel shows the cloud for $K_{zz}=10^8 \text{ cm}^2 \text{ s}^{-1}$ and the right hand side panel for $K_{zz}=10^6 \text{ cm}^2 \text{ s}^{-1}$.

extremely efficient. However, their abundances drop quickly with altitude. This separation into three layers disappears at $K_{zz} \sim 10^8 \text{ cm}^2 \text{ s}^{-1}$. Only the lowest Mg-oxide layer can be distinguished from a more extended upper layer, where $\text{TiO}_2(\text{s})$ is the major component mixed with other components including silicates and iron oxides. The cloud particles reach their maximal grain sizes of $\approx 0.1 \mu\text{m}$ around 0.01 bar. Towards the cloud top, the particles shrink to $0.03 \mu\text{m}$ diameter. The overall particle size increases with K_{zz} , because the gas replenishment becomes faster leading to quicker particle growth, see Figure 3.3. In the case of strongest mixing $K_{zz} \sim 10^{10} \text{ cm}^2$, grain sizes vary between 0.23 and $0.13 \mu\text{m}$.

Figure 14 illustrates how the differences in the cloud structure due to changes in vertical mixing affect the transmission features of the cloud. The cloud features become weaker with smaller K_{zz} because the entire cloud is optically thinner. The drop off in the optical slope happens at shorter wavelengths because the small particles in

weakly mixed atmospheres scatter shorter wavelengths compared to the larger particles in highly mixed atmospheres.

4 DISCUSSION

4.1 Outgassed atmospheres

The ability to form a certain condensate depends on the availability of the limiting species. Increasing its abundance can increase the condensate abundance and the condensation temperature. Therefore, it depends on the availability of refractory species which clouds we can expect. [van Buchem et al. \(2023, 2024\)](#); [Zilinskas et al. \(2022\)](#) show that outgassing from a molten surface can enhance the gas phase abundances of SiO , SiO_2 and TiO . This would lead to the formation of atmospheres as predicted by [Zilinskas et al. \(2022\)](#); [Piette et al. \(2023\)](#); [Seidler et al. \(2024\)](#) where SiO strongly affects the temperature structure. [Zilinskas et al. \(2022\)](#) find that the three

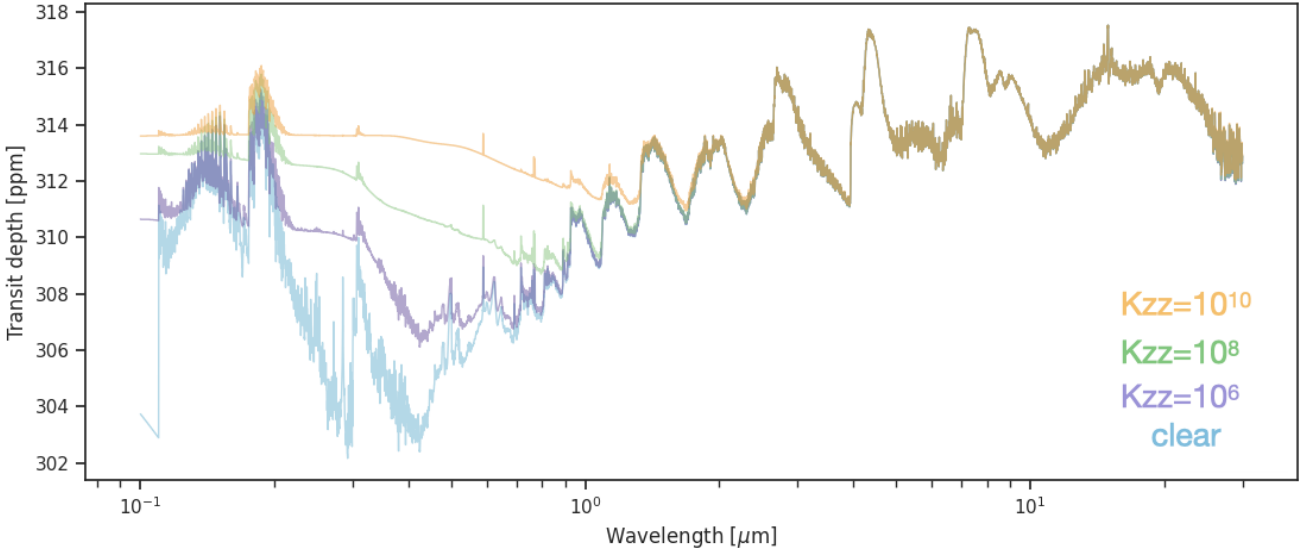


Figure 14. Transmission spectrum of the O_2/CO_2 atmosphere Figure 2 model 5. Shown are features between $0.1 - 30 \mu\text{m}$. The blue spectrum is simulated without any cloud opacities. The orange, green and purple spectra are cloudy with different strengths of eddy diffusion, $K_{zz} 10^{10} \text{ cm}^2 \text{ s}^{-1}$, $K_{zz} 10^8 \text{ cm}^2 \text{ s}^{-1}$ and $K_{zz} 10^6 \text{ cm}^2 \text{ s}^{-1}$ respectively. For each eddy diffusion parameter, the corresponding clouds are shown in sections 3.3.1 and 3.5. The stronger the vertical mixing, the stronger the cloud affects the spectrum.

species are key in forming the temperature structure in outgassed atmospheres and can give rise to strong features in emission spectra. They highlight that SiO can be used as a tracer of magma oceans. These molecules can be the limiting species for forming silicon- or titanium condensates and therefore their abundance impacts to what extent cloud formation can take place in such atmospheres. The other way around, cloud formation can deplete SiO , SiO_2 and TiO in planetary atmospheres and therefore potentially diminish their effect on temperature structure and observability. We will investigate the extent of this effect in a future study.

Within the scope of what we have investigated in this work, we find that in the range of considered compositions, O-dominated atmospheres are particularly prone towards cloud formation due to their low temperatures at high altitudes. Gkouvelis et al. (2025) show that due to their higher mean molecular weight, O_2 -atmospheres around small planets are also less likely to escape compared to H_2 -atmospheres. Cherubim et al. (2025) further suggest a trend in sub-Neptunes and super-Earths that smaller planets are more oxidised compared to larger planets. If a sub-Neptune has a H-rich envelope, this envelope pushes water to be trapped in the magma ocean (e.g. Kite et al. 2019, 2020; Dorn & Lichtenberg 2021; Gaillard et al. 2022; Sossi et al. 2023). After the loss of this envelope, H_2O is outgassed and the gaseous hydrogen escapes leaving an oxidised atmosphere behind. Therefore, we would expect these small, evolved planets to be particularly relevant for the observations of clouds on strongly irradiated planets. In a similar way to H_2O , we also expect that the species which rain out at the surface of the atmosphere would dissolve into the melt to some extent. Our current models assume that solid and liquid species which rain out stay on the surface. Outgassing codes like LavAtmos (van Buchem et al. 2023, 2024) can model gas-magma interactions without considering dissolution into the melt. Integrating the latter for a wide range of rained out condensates would be novel and crucial to consider in the future in order to fully understand the physics and chemistry of cloudy super-Earths and sub-Neptunes.

4.2 55 Cnc e

Clouds can also have a cooling effect on the atmosphere. Loftus et al. (2024) propose a cyclical pattern between cooling by clouds and reheating of the atmosphere after cloud dissipation to be a potential source for the observed variability on 55 Cnc e (Demory et al. 2016). Our results suggest that this would mainly happen in the case of an oxygen rich atmosphere, since these are the atmospheres most prone to cloud formation. However, further analysis is needed to confirm this. We will investigate the role of clouds for potential variability in a future work.

We have shown that one likely cloud composition on 55 Cnc e are titanium clouds. However, depending on the surface pressure, on the composition of a potential primary volatile envelope as well as on the magma composition, the available cloud materials can differ drastically from what we find with solar refractory abundances (Gaillard & Scaillet 2014; van Buchem et al. 2023, 2024). Thus, clouds on magma oceans planets like 55 Cnc e could be of a much greater variety. It remains to be discovered, whether 55 Cnc e hosts clouds and if so, what they are made of.

4.3 Availability of optical data

So far, research on cloud formation above 1500 K has been predominantly focusing on hydrogen-dominated atmospheres [e.g.] (Powell & Zhang 2024; Helling & Woitke 2006; Helling et al. 2008; Wakeford & Sing 2015; Helling et al. 2017; Huang et al. 2024; Bell et al. 2024). Helling et al. (2008) list reaction rates for $\text{TiO}_2(\text{s})$, $\text{CaTiO}_3(\text{s})$, $\text{Al}_2\text{O}_3(\text{s})$, $\text{Mg}_2\text{SiO}_4(\text{s})$, $\text{MgSiO}_3(\text{s})$, $\text{MgO}(\text{s})$, $\text{Fe}_2\text{O}_3(\text{s})$, $\text{FeS}(\text{s})$, $\text{FeO}(\text{s})$, $\text{Fe}(\text{s})$, $\text{SiO}(\text{s})$ and $\text{SiO}_2(\text{s})$. In Helling et al. (2017) additional reaction pathways for carbon bearing species $\text{C}(\text{s})$, $\text{SiC}(\text{s})$, $\text{TiC}(\text{s})$ and for $\text{KCl}(\text{s})$ and $\text{MgS}(\text{s})$ are available. Wakeford et al. (2017) focus on high temperature condensates classifying them into Ti- bearing and Al-bearing species. Our findings suggest that further cloud species beyond those mentioned can be relevant. For example, $\text{MgTi}_2\text{O}_5(\text{s}, \text{l})$ and $\text{Mg}_2\text{TiO}_4(\text{s}, \text{l})$ can become major com-

ponents of cloud particles in O-dominated atmospheres or in H- and N-dominated atmospheres with $C/O < 1$, although, we don't find $Mg_2TiO_4(s, l)$ with abundances > 1 ppb in N-dominated atmospheres with $C/O 0.5$. In addition, $Fe_3O_4(s, l)$ needs to be considered for O- and N-dominated atmospheres with $C/O < 1$. Recently, also phosphorus has received more attention. [Zilinskas et al. \(2025\)](#) mention the possibility that 55 Cnc e could have a phosphorus rich atmosphere. We find that an atmosphere with abundant sulphur and phosphorus is not a favourable environment for condensation if it is H-dominated. However, in O-atmospheres which are rich in sulphur and phosphorus, PO_2 can condense to form $(P_2O_5)_2(s)$ or $Mg_3(PO_4)_2(s)$ if magnesium is available. $Mg_3(PO_4)_2(s)$ can also form in N-atmospheres with low C/O ratio and low H/O ratio. No measured refractive indices for condensate species with P-O stretch are available. Thus, more optical data is needed for more accurate predictions of the spectral features of clouds in oxygen rich atmospheres. In addition, there is also a lack data for high C/O atmospheres. In some of these N-atmospheres, $TiN(s)$ and $AlN(s)$ clouds can form, but no optical data is available for species with Ti-N or Al-N features yet. Furthermore, optical constants used to identify spectral features of cloud particles are a function of temperature ([Luna & Morley 2021](#)). The data we use has been taken at temperatures < 1000 K. However, we consider much hotter atmospheres with temperatures ranging up to 3000 K at the surface. Optical data for such hot regimes is not available. This adds uncertainty to the prediction of the features for all the considered materials. Similarly, some solid materials also have different temperature, pressure and composition dependent morphologies which we don't account for, as mentioned in section 3.4. To interpret spectral features in atmospheres of hot sub-Neptunes and super-Earths correctly it is advantageous to have optical constants ranging from the UV to the infrared at temperatures at least up to 3000 K for different morphology types of all major cloud materials mentioned in this work.

4.4 Spectral features

In section 3.4.2 we show the spectrum for one specific case of O_2/CO_2 atmospheres. However, the spectral features which will appear are very dependent on the atmospheric composition and the temperature structure. We expect O_2 -dominated atmospheres to have small scale heights. If refractories are outgassed, this could increase the atmospheric weight even further. In this case, a flattening effect of clouds could be degenerate with a very heavy atmosphere. Features in transmission will be difficult to see. Given the fact that we expect most small planets to have oxygen rich atmospheres (e.g. [Cherubim et al. 2025](#)), this makes the characterisation of their atmospheres difficult. We will investigate observability further in future work.

4.5 Model caveats and future improvements

In addition to better optical data, our model itself could also benefit from some refinements in the future. So far, our model accounts for gas phase chemistry and condensation reactions but no solid-solid reactions. Common materials we find in the solar environment medium are forsterite and enstatite enhanced with iron ([Jaeger et al. 1994](#)). We only consider fayalite, pure forsterite, pure enstatite and iron-oxides $FeO(s)$, $Fe_2O_3(s)$ and $Fe_3O_4(s)$. Solid-solid reactions could potentially be the cause for the formation of further materials and alter the relative abundances of already present species.

The effect of scattering and absorption by aerosol particles on the temperature structure is another major mechanism which also

needs to be considered to understand the feedback between clouds, atmosphere and surface-atmosphere interactions. Investigating this is beyond the scope of this paper but remains a source of uncertainty in our models.

It is also to note that we have chosen a particular irradiation of the planet which correspond to the irradiation received by 55 Cnc e scaled with a heat redistribution factor of $\frac{1}{3}$. The obtained results will be altered if the planetary parameters or the location on the planet (dayside, terminators, nightside) change. In general, planetary terminators tend to be cooler compared to their day sides. This could enhance cloud formation in these regions compared to our predictions. In addition, horizontal atmospheric movements can lead to asymmetries in planetary atmospheres, which further promotes cloud formation at the planet's terminators e.g. ([Lee 2023](#)).

5 CONCLUSIONS

We have developed a model which couples gas-phase chemistry with radiative transfer and a cloud formation model to investigate the types of clouds that may form in the atmospheres of hot (> 2000 K) sub-Neptunes and super-Earths. We conclude the following:

- (i) Depending on the composition, different molecules acting as heating agents can form in oxygen poor atmospheres. These are mainly TiO , CN - if nitrogen and carbon are abundant -, and PS - if phosphorus and sulphur are abundant. These species are strong absorbers in the optical and UV ranges and can cause temperature inversions, inhibiting cloud formation.
- (ii) Oxygen rich atmospheres (O-dominated or oxygen enriched H- and N-atmospheres with $C/O < 1$) are more conducive to cloud formation. The presence of oxygen enables the formation of a wider range of condensates, and these atmospheres are generally cooler, presenting better conditions for cloud formation.
- (iii) A detailed cloud model is essential for accurate cloud characterisation. Equilibrium condensation with rainout underestimates both the cloud mass and the vertical extent of clouds, particularly those forming at lower altitudes.
- (iv) Vertical mixing has a substantial impact on cloud properties. Stronger vertical mixing leads to larger cloud particles, more extended and uniform cloud decks, and more prominent spectral features.
- (v) TiO_2 is the dominant cloud species expected in a O_2/CO_2 -dominated atmosphere with a solar refractory element composition.
- (vi) O_2/CO_2 atmospheres are heavy, making their spectral features weaker. In the infrared, clouds have little impact on the transmission spectrum. However, in the optical and in the UV they can mute features of some gaseous species like OH .
- (vii) Cloud species can be grouped according to their spectral features. Their features are the strongest in the UV and optical, where the slope has unique properties. However, it is crucial to account for degeneracies between particle size, mean molecular weight and cloud species to analyse observed features at these wavelengths. TiO species have a unique feature between $0.2 - 0.3 \mu m$ and SiO species between $0.1 - 0.2 \mu m$. Fe -species can produce a shallow, high opacity slope, between $0.1 - 15 \mu m$. Graphite - $C(s)$ - has a relatively strong extinction throughout a broad wavelength range from $0.1 - 30 \mu m$, leading to a prominent flattening effect of graphite clouds in transmission spectra.

In summary, the oxygen abundance of a planetary atmosphere plays a critical role in its thermal structure and cloud formation. Clouds are predominantly present in oxidised atmospheres of hot

sub-Neptune sized planets and can span a variety of compositions. Our findings show that we cannot neglect cloud formation in hot atmospheres as clouds leave imprints on atmospheric climates and planetary spectra. To optimise the analysis of future observations, more detailed models including outgassing from a magma ocean and the impact of clouds on the temperature structure as well as further optical data for solid and liquid species are essential.

ACKNOWLEDGEMENTS

Many thanks to Billy Edwards for fantastic advice on histograms. L.J.J and Y.M acknowledge support from the European Research Council (ERC) under the European Union's Horizon 2020 research and innovation programme (grant agreement no. 101088557, NGINE).

DATA AVAILABILITY

All data will be available upon request. We conducted our work with open source codes HELIOS <https://github.com/HELIOS-framework/HELIOS>, FASTCHEM3 <https://github.com/NewStrangeWorlds/FastChem>, OPTOOL <https://github.com/cdominik/optool>, and ExoLYN <https://github.com/helonguangastro/ExoLyn>.

REFERENCES

Adam A. Y., Yachmenev A., Yurchenko S. N., Jensen P., 2019, *Journal of Physical Chemistry A*, **123**, 4755

Al-Refaei A. F., Yachmenev A., Tennyson J., Yurchenko S. N., 2015, *MNRAS*, **448**, 1704

Al-Refaei A. F., Polyansky O. L., Ovsyannikov R. I., Tennyson J., Yurchenko S. N., 2016, *MNRAS*, **461**, 1012

Amaral P. H. R., Diniz L. G., Jones K. A., Stanke M., Alijah A., Adamowicz L., Mohallem J. R., 2019, *ApJ*, **878**, 95

August P. C., et al., 2025, *A&A*, **695**, A171

Azzam A. A. A., Tennyson J., Yurchenko S. N., Naumenko O. V., 2016, *MNRAS*, **460**, 4063

Barber R. J., Strange J. K., Hill C., Polyansky O. L., Mellau G. C., Yurchenko S. N., Tennyson J., 2014, *MNRAS*, **437**, 1828

Bean J. L., Raymond S. N., Owen J. E., 2021, *Journal of Geophysical Research (Planets)*, **126**, e06639

Bell T. J., et al., 2024, *Nature Astronomy*, **8**, 879

Bernath P. F., 2020, *J. Quant. Spectrosc. Radiative Transfer*, **240**, 106687

Borysow A., 2002, *A&A*, **390**, 779

Borysow A., Jorgensen U. G., Fu Y., 2001, *J. Quant. Spectrosc. Radiative Transfer*, **68**, 235

Bourrier V., et al., 2018, *A&A*, **619**, A1

Brady R. P., Yurchenko S. N., Tennyson J., Kim G.-S., 2024, *MNRAS*, **527**, 6675

Burn R., Mordasini C., Mishra L., Haldemann J., Venturini J., Emsenhuber A., Henning T., 2024, *Nature Astronomy*, **8**, 463

Burrows A., Dulick M., Bauschlicher C. W. J., Bernath P. F., Ram R. S., Sharp C. M., Milsom J. A., 2005, *ApJ*, **624**, 988

Carone L., Lewis D. A., Samra D., Schneider A. D., Helling C., 2023, *arXiv e-prints*, p. arXiv:2301.08492

Cherubim C., Wordsworth R., Bower D., Sossi P., Adams D., Hu R., 2025, *arXiv e-prints*, p. arXiv:2503.05055

Chubb K. L., Tennyson J., Yurchenko S. N., 2020, *MNRAS*, **493**, 1531

Clark V. H. J., Owens A., Tennyson J., Yurchenko S. N., 2020, *J. Quant. Spectrosc. Radiative Transfer*, **246**, 106929

Coles P. A., Yurchenko S. N., Tennyson J., 2019, *MNRAS*, **490**, 4638

Crida A., Ligi R., Dorn C., Borsa F., Lebreton Y., 2018, *Research Notes of the American Astronomical Society*, **2**, 172

Dang L., et al., 2024, in AASTCS10, Extreme Solar Systems V. p. 103.02

Dang L., et al., 2025, Surveying Hellish Worlds: Lava Planets as Time Capsules of Thermal Evolution, JWST Proposal. Cycle 4, ID. #8864

Demory B.-O., Gillon M., Madhusudhan N., Queloz D., 2016, *MNRAS*, **455**, 2018

Dominik C., Min M., Tazaki R., 2021, Astrophysics Source Code Library, record ascl:2104.010,

Dorn C., Lichtenberg T., 2021, *ApJ*, **922**, L4

Dragomir D., Matthews J. M., Winn J. N., Rowe J. F., 2014, in Haghighipour N., ed., IAU Symposium Vol. 293, Formation, Detection, and Characterization of Extrasolar Habitable Planets. pp 52–57 (arXiv:1302.3321), doi:10.1017/S1743921313012520

Draine B. T., 2003, *ApJ*, **598**, 1017

Ducrot E., et al., 2025, *Nature Astronomy*, **9**, 358

Dulick M., Bauschlicher C. W. J., Burrows A., Sharp C. M., Ram R. S., Bernath P., 2003, *ApJ*, **594**, 651

Essack Z., Seager S., Pajusala M., 2020, *ApJ*, **898**, 160

Fabian D., Henning T., Jäger C., Mutschke H., Dorschner J., Wehrhan O., 2001, *A&A*, **378**, 228

Fernando A. M., Bernath P. F., Hodges J. N., Masseron T., 2018, *J. Quant. Spectrosc. Radiative Transfer*, **217**, 29

Fulton B. J., et al., 2017, *AJ*, **154**, 109

Gaillard F., Scaillet B., 2014, *Earth and Planetary Science Letters*, **403**, 307

Gaillard F., et al., 2022, *Earth and Planetary Science Letters*, **577**, 117255

Gao P., et al., 2020, *Nature Astronomy*, **4**, 951

Gardner J. P., et al., 2006, *Space Sci. Rev.*, **123**, 485

GharibNezhad E., Shayesteh A., Bernath P. F., 2013, *MNRAS*, **432**, 2043

Ginzburg S., Schlichting H. E., Sari R., 2018, *MNRAS*, **476**, 759

Gkouvelis L., Pozuelos F. J., Drant T., Farhat M., Tian M., Akin C., 2025, *arXiv e-prints*, p. arXiv:2506.02188

Gorman M. N., Yurchenko S. N., Tennyson J., 2019, *MNRAS*, **490**, 1652

Grant D., et al., 2023, *ApJ*, **956**, L32

Gray D. F., 2008, *The Observation and Analysis of Stellar Photospheres*. Cambridge University press

Hammond M., Pierrehumbert R. T., 2017, *ApJ*, **849**, 152

Hargreaves R. J., et al., 2019, *J. Quant. Spectrosc. Radiative Transfer*, **232**, 35

Helling C., 2019, *Annual Review of Earth and Planetary Sciences*, **47**, 583

Helling C., Woitke P., 2006, *A&A*, **455**, 325

Helling C., Woitke P., Thi W. F., 2008, *A&A*, **485**, 547

Helling C., Tootill D., Woitke P., Lee E., 2017, *A&A*, **603**, A123

Heng K., 2023, *ApJ*, **956**, L20

Heng K., Demory B.-O., 2013, *ApJ*, **777**, 100

Heng K., Owen J. E., Tian M., 2025, *arXiv e-prints*, p. arXiv:2504.02499

Henning T., Mutschke H., 1997, *A&A*, **327**, 743

Henning T., Mutschke H., 2001, *Spectrochimica Acta Part A: Molecular Spectroscopy*, **57**, 815

Henning T., Begemann B., Mutschke H., Dorschner J., 1995, *A&AS*, **112**, 143

Hinkel N. R., Timmes F. X., Young P. A., Pagano M. D., Turnbull M. C., 2014, *AJ*, **148**, 54

Hodges J. N., Bernath P. F., 2017, *ApJ*, **840**, 81

Hu R., et al., 2024, *Nature*, **630**, 609

Huang H., Ormel C. W., Min M., 2024, *A&A*, **691**, A291

Husser T. O., Wende-von Berg S., Dreizler S., Homeier D., Reiners A., Barman T., Hauschildt P. H., 2013, *A&A*, **553**, A6

Izidoro A., Schlichting H. E., Isella A., Dasgupta R., Zimmermann C., Bitsch B., 2022, *ApJ*, **939**, L19

Jaeger C., Mutschke H., Begemann B., Dorschner J., Henning T., 1994, *A&A*, **292**, 641

Jäger C., Dorschner J., Mutschke H., Posch T., Henning T., 2003, *A&A*, **408**, 193

John T. L., 1988, *A&A*, **193**, 189

Karman T., et al., 2019, *Icarus*, **328**, 160

Kiefer S., Samra D., Lewis D. A., Schneider A. D., Min M., Carone L., Decin L., Helling C., 2024, *A&A*, **690**, A244

Kite E. S., Fegley Jr. B., Schaefer L., Ford E. B., 2019, *ApJ*, **887**, L33
 Kite E. S., Fegley Jr. B., Schaefer L., Ford E. B., 2020, *ApJ*, **891**, 111
 Kitzmann D., Heng K., 2018, *MNRAS*, **475**, 94
 Kitzmann D., Stock J. W., Patzer A. B. C., 2024, *MNRAS*, **527**, 7263
 Kofman V., Villanueva G. L., 2021, *J. Quant. Spectrosc. Radiative Transfer*, **270**, 107708
 Koike C., Kaito C., Yamamoto T., Shibai H., Kimura S., Suto H., 1995, *Icarus*, **114**, 203
 Kreidberg L., et al., 2014, *Nature*, **505**, 69
 Kuchner M. J., Seager S., 2005, *arXiv e-prints*, pp astro-ph/0504214
 Kurucz R. L., 1992, *Rev. Mex. Astron. Astrofis.*, **23**, 45
 Langley J., Tennyson J., Yurchenko S. N., Bernath P., 2019, *MNRAS*, **488**, 2332
 Laor A., Drain B. T., 1993, *ApJ*, **402**, 441
 Lee E. K. H., 2023, *MNRAS*, **524**, 2918
 Lellouch E., McGrath M. A., Jessup K. L., 2007, in Lopes R. M. C., Spencer J. R., eds., *Io After Galileo: A New View of Jupiter's Volcanic Moon*. Springer Praxis Books / Geophysical Sciences, p. 231, doi:10.1007/978-3-540-48841-5_10
 Li G., Garrison J. J., Ram R. S., Western C. M., Bernath P. F., 2012, *J. Quant. Spectrosc. Radiative Transfer*, **113**, 67
 Li G., Gordon I. E., Rothman L. S., Tan Y., Hu S.-M., Kassi S., Campargue A., Medvedev E. S., 2015, *ApJS*, **216**, 15
 Li H. Y., Tennyson J., Yurchenko S. N., 2019, *MNRAS*, **486**, 2351
 Lichtenberg T., Miguel Y., 2025a, *Treatise on Geochemistry*, **7**, 51
 Lichtenberg T., Miguel Y., 2025b, *Treatise on Geochemistry*, **7**, 51
 Lodders K., 2019, *arXiv e-prints*, p. arXiv:1912.00844
 Loftus K., Luo Y., Fan B., Kite E. S., 2024, *arXiv e-prints*, p. arXiv:2409.16270
 Luna J. L., Morley C. V., 2021, *ApJ*, **920**, 146
 Luque R., Pallé E., 2022, *Science*, **377**, 1211
 Mahapatra G., Helling C., Miguel Y., 2017, *MNRAS*, **472**, 447
 Malik M., et al., 2017, *AJ*, **153**, 56
 Malik M., Kitzmann D., Mendonça J. M., Grimm S. L., Marleau G.-D., Linder E. F., Tsai S.-M., Heng K., 2019a, *AJ*, **157**, 170
 Malik M., Kempton E. M. R., Koll D. D. B., Mansfield M., Bean J. L., Kite E., 2019b, *ApJ*, **886**, 142
 Mant B. P., Yachmenev A., Tennyson J., Yurchenko S. N., 2018, *MNRAS*, **478**, 3220
 Masseron T., et al., 2014, *A&A*, **571**, A47
 McKemmish L. K., Masseron T., Hoeijmakers H. J., Pérez-Mesa V., Grimm S. L., Yurchenko S. N., Tennyson J., 2019, *MNRAS*, **488**, 2836
 Meier Valdés E. A., et al., 2023, *A&A*, **677**, A112
 Meier Valdés E. A., et al., 2025, *arXiv e-prints*, p. arXiv:2503.19772
 Min M., Hovenier J. W., de Koter A., 2005, *A&A*, **432**, 909
 Mitev G. B., Taylor S., Tennyson J., Yurchenko S. N., Buchachenko A. A., Stolyarov A. V., 2022, *MNRAS*, **511**, 2349
 Mollière P., Wardenier J. P., van Boekel R., Henning T., Molaverdikhani K., Snellen I. A. G., 2019, *A&A*, **627**, A67
 Moran S. E., Marley M. S., Crossley S. D., 2024, *ApJ*, **973**, L3
 Ormel C. W., Min M., 2019, *A&A*, **622**, A121
 Owen J. E., Wu Y., 2013, *ApJ*, **775**, 105
 Owens A., Yachmenev A., Thiel W., Tennyson J., Yurchenko S. N., 2017, *MNRAS*, **471**, 5025
 Owens A., Conway E. K., Tennyson J., Yurchenko S. N., 2020, *MNRAS*, **495**, 1927
 Owens A., Tennyson J., Yurchenko S. N., 2021, *MNRAS*, **502**, 1128
 Owens A., Mitrushchenkov A., Yurchenko S. N., Tennyson J., 2022, *MNRAS*, **516**, 3995
 Owens A., Yurchenko S. N., Tennyson J., 2024, *MNRAS*, **530**, 4004
 Palik E. D., 1985, *Handbook of optical constants of solids*. Academic Press Handbook Series, New York: Academic Press
 Palik E. D., 1991, *Handbook of optical constants of solids II*. Boston: Academic Press
 Patrasec A. T., Yurchenko S. N., Tennyson J., 2015, *MNRAS*, **449**, 3613
 Paulose G., Barton E. J., Yurchenko S. N., Tennyson J., 2015, *MNRAS*, **454**, 1931
 Pavlyuchko A. I., Yurchenko S. N., Tennyson J., 2015, *MNRAS*, **452**, 1702
 Piette A. A. A., Gao P., Brugman K., Shahar A., Lichtenberg T., Miozzi F., Driscoll P., 2023, *ApJ*, **954**, 29
 Pinhas A., Madhusudhan N., 2017, *MNRAS*, **471**, 4355
 Pollack J. B., Hollenbach D., Beckwith S., Simonelli D. P., Roush T., Fong W., 1994, *ApJ*, **421**, 615
 Polyansky O. L., Kyuberis A. A., Zobov N. F., Tennyson J., Yurchenko S. N., Lodi L., 2018, *MNRAS*, **480**, 2597
 Posch T., Kerschbaum F., Fabian D., Mutschke H., Dorschner J., Tamanai A., Henning T., 2003, *ApJS*, **149**, 437
 Powell D., Zhang X., 2024, *ApJ*, **969**, 5
 Prajapat L., Jagoda P., Lodi L., Gorman M. N., Yurchenko S. N., Tennyson J., 2017, *MNRAS*, **472**, 3648
 Qin Z., Bai T., Liu L., 2021, *J. Quant. Spectrosc. Radiative Transfer*, **258**, 107352
 Qu Q., Yurchenko S. N., Tennyson J., 2021, *MNRAS*, **504**, 5768
 Ram R. S., Brooke J. S. A., Western C. M., Bernath P. F., 2014, *J. Quant. Spectrosc. Radiative Transfer*, **138**, 107
 Rauer H., et al., 2025, *Experimental Astronomy*, **59**, 26
 Redfield S., et al., 2024, *arXiv e-prints*, p. arXiv:2404.02932
 Rivlin T., Lodi L., Yurchenko S. N., Tennyson J., Le Roy R. J., 2015, *MNRAS*, **451**, 634
 Rothman L. S., et al., 2010, *J. Quant. Spectrosc. Radiative Transfer*, **111**, 2139
 Ryabchikova T., Piskunov N., Kurucz R. L., Stempels H. C., Heiter U., Pakhomov Y., Barklem P. S., 2015, *Phys. Scr.*, **90**, 054005
 Seidler F. L., Sossi P. A., Grimm S. L., 2024, *A&A*, **691**, A159
 Seidler F. L., Sossi P. A., Bower D. J., Demory B.-O., 2025, *arXiv e-prints*, p. arXiv:2509.13610
 Semenov M., Clark N., Yurchenko S. N., Kim G.-S., Tennyson J., 2022, *MNRAS*, **516**, 1158
 Semenov M., El-Kork N., Yurchenko S. N., Tennyson J., 2025, *MNRAS*, **536**, 714
 Sossi P. A., Tolland P. M. E., Badro J., Bower D. J., 2023, *Earth and Planetary Science Letters*, **601**, 117894
 Sousa-Silva C., Al-Refaie A. F., Tennyson J., Yurchenko S. N., 2015, *MNRAS*, **446**, 2337
 Stock J. W., Kitzmann D., Patzer A. B. C., Sedlmayr E., 2018, *MNRAS*, **479**, 865
 Syme A.-M., McKemmish L. K., 2021, *MNRAS*, **505**, 4383
 Tennyson J., et al., 2024, *J. Quant. Spectrosc. Radiative Transfer*, **326**, 109083
 Tinetti G., et al., 2018, *Experimental Astronomy*, **46**, 135
 Underwood D. S., Tennyson J., Yurchenko S. N., Huang X., Schwenke D. W., Lee T. J., Clausen S., Fateev A., 2016a, *MNRAS*, **459**, 3890
 Underwood D. S., Yurchenko S. N., Tennyson J., Al-Refaie A. F., Clausen S., Fateev A., 2016b, *MNRAS*, **462**, 4300
 Upadhyay A., Conway E. K., Tennyson J., Yurchenko S. N., 2018, *MNRAS*, **477**, 1520
 Venot O., Drummond B., Miguel Y., Waldmann I. P., Pascale E., Zingales T., 2018, *Experimental Astronomy*, **46**, 101
 Wakeford H. R., Sing D. K., 2015, *A&A*, **573**, A122
 Wakeford H. R., Visscher C., Lewis N. K., Kataria T., Marley M. S., Fortney J. J., Mandell A. M., 2017, *MNRAS*, **464**, 4247
 Western C. M., Carter-Blatchford L., Crozet P., Ross A. J., Morville J., Tokaryk D. W., 2018, *J. Quant. Spectrosc. Radiative Transfer*, **219**, 127
 Whittaker E. A., et al., 2022, *AJ*, **164**, 258
 Wong A., Yurchenko S. N., Bernath P., Müller H. S. P., McConkey S., Tennyson J., 2017, *MNRAS*, **470**, 882
 Yurchenko S. N., Blissett A., Asari U., Vasilios M., Hill C., Tennyson J., 2016, *MNRAS*, **456**, 4524
 Yurchenko S. N., Amundsen D. S., Tennyson J., Waldmann I. P., 2017, *A&A*, **605**, A95
 Yurchenko S. N., Sinden F., Lodi L., Hill C., Gorman M. N., Tennyson J., 2018a, *MNRAS*, **473**, 5324
 Yurchenko S. N., Bond W., Gorman M. N., Lodi L., McKemmish L. K., Nunn W., Shah R., Tennyson J., 2018b, *MNRAS*, **478**, 270
 Yurchenko S. N., Williams H., Leyland P. C., Lodi L., Tennyson J., 2018c, *MNRAS*, **479**, 1401

Yurchenko S. N., Szabó I., Pyatenko E., Tennyson J., 2018d, [MNRAS](#), **480**, 3397

Yurchenko S. N., Tennyson J., Miller S., Melnikov V. V., O'Donoghue J., Moore L., 2020, [MNRAS](#), **497**, 2340

Yurchenko S. N., et al., 2022, [MNRAS](#), **510**, 903

Zeidler S., Posch T., Mutschke H., Richter H., Wehrhan O., 2011, [A&A](#), **526**, A68

Zeidler S., Posch T., Mutschke H., 2013, [A&A](#), **553**, A81

Zieba S., et al., 2023, [Nature](#), **620**, 746

Zilinskas M., Miguel Y., Molière P., Tsai S.-M., 2020, [MNRAS](#), **494**, 1490

Zilinskas M., van Buchem C. P. A., Miguel Y., Louca A., Lupu R., Zieba S., van Westrenen W., 2022, [A&A](#), **661**, A126

Zilinskas M., Miguel Y., van Buchem C. P. A., Snellen I. A. G., 2023, [arXiv e-prints](#), p. [arXiv:2301.05190](#)

Zilinskas M., et al., 2025, [A&A](#), **697**, A34

van Buchem C. P. A., Miguel Y., Zilinskas M., van Westrenen W., 2023, [maps](#), **58**, 1149

van Buchem C. P. A., Zilinskas M., Miguel Y., van Westrenen W., 2024, [arXiv e-prints](#), p. [arXiv:2408.10863](#)

APPENDIX A: OPACITY REFERENCES

This paper has been typeset from a $\text{\TeX}/\text{\LaTeX}$ file prepared by the author.

Table A1. Opacities

Species	Source	use	Line list	Line List Reference
Al	DACE/ExoMol	RT/TS	VALD/Kurucz	Ryabchikova et al. (2015); Kurucz (1992)
AlH	HELIOS-K/ExoMol	RT/TS	AlHambra	Yurchenko et al. (2018c)
AlO	HELIOS-K/ExoMol	RT/TS	ATP	Patrascu et al. (2015)
C ₂ H ₂	DACE/ExoMol	RT/TS	aCeTY	Chubb et al. (2020)
C ₂ H ₄	DACE/ExoMol	RT/TS	MaTY	Mant et al. (2018)
Ca	DACE/ExoMol	RT/TS	VALD/Kurucz	Ryabchikova et al. (2015); Kurucz (1992)
CaH	HELIOS-K/ExoMol	RT/TS	MoLLIST	Li et al. (2012); Bernath (2020)
CaO	HELIOS-K	RT	VBATHY	Yurchenko et al. (2016)
CaOH	DACEExoMol	RT/TS	OYT6	Owens et al. (2022)
C ₂	DACEExoMol	RT/TS	8states	Yurchenko et al. (2018d)
CH	DACE	RT	MoLLIST	Masseron et al. (2014); Bernath (2020)
CH ₃	DACE	RT	AYYJ	Adam et al. (2019)
CH ₄	DACE/ExoMol	RT/TS	YT34to10/MM	Yurchenko et al. (2017)
CN	HELIOS-K/ExoMol	RT/TS	Trihybrid/MoLLIST	Syme & McKemmish (2021)
CO	DACE/ExoMol	RT/TS	Li2015/HITEMP	Li et al. (2015)
CO ₂	DACE/ExoMol	RT/TS	HITEMP/UCL-4000m	Rothman et al. (2010); Yurchenko et al. (2020)
CS	DACE/ExoMol	RT/TS	JnK	Paulose et al. (2015)
Fe	DACE/ExoMol	RT/TS	VALD/Kurucz	Ryabchikova et al. (2015); Kurucz (1992)
FeH	DACE/ExoMol	RT/TS	MoLLIST	Dulick et al. (2003)
H ₂ ⁺	DACE	RT	ADJSAM	Amaral et al. (2019)
H ₂ O	DACE/ExoMol	RT/TS	POKAZATEL	Polyansky et al. (2018)
H ₂ O ₂	DACE	RT	APTY	Al-Refaie et al. (2016)
H ₂ CO	DACE	RTS	AYTY	Al-Refaie et al. (2015)
H ₂ S	DACE/ExoMol	RT	AYT2	Azzam et al. (2016)
H ₃ O ⁺	DACE	RT	eXeL	Yurchenko et al. (2020)
HCN	HELIOS-K/ExoMol	RT/TS	Harris	Barber et al. (2014)
HNO ₃	DACE	RT/TS	AIJS	Pavlyuchko et al. (2015)
HS	HELIOS-K/ExoMol	RT/TS	GYT	Gorman et al. (2019)
K	DACE/ExoMol	RT/TS	VALD/Kurucz	Ryabchikova et al. (2015); Kurucz (1992)
KOH	DACE	RT/TS	OYT4	Owens et al. (2021)
Mg	DACE/ExoMol	RT/TS	Kurucz	Kurucz (1992)
MgH	HELIOS-K/ExoMol	RT/TS	MoLLIST	GharibNezhad et al. (2013); Bernath (2020)
MgO	HELIOS-K/ExoMol	RT/TS	LiTY	Li et al. (2019)
N ₂	DACE/ExoMol	RT/TS	WCCRMT	Western et al. (2018)
N ₂ O	DACE	RT/TS	HITEMP2019/TYM	Hargreaves et al. (2019)
Na	DACE/ExoMol	RT/TS	VALD/Kurucz	Ryabchikova et al. (2015); Kurucz (1992)
NaH	HELIOS-K/ExoMol	RT/TS	Rivlin	Rivlin et al. (2015)
NaO	DACE	RT	NaOUCMe	Mitev et al. (2022)
NaOH	DACE/ExoMol	RT/TS	OYT5	Owens et al. (2021)
NH	DACE	RT	MoLLIST	Fernando et al. (2018)
NH ₃	DACE/ExoMol	RT/TS	CoYuTe	Coles et al. (2019)
NO	DACE	RT	XABC	Wong et al. (2017); Qu et al. (2021)
NS	DACE	RT	SNaSH	Yurchenko et al. (2018b)
OH	DACE/ExoMol	RT/TS	HITEMP/MoLLIST	Rothman et al. (2010)
OH ⁺	DACE	RT	MoLLIST	Hodges & Bernath (2017)
PC	DACE/ExoMol	RT/TS	MoLLIST	Ram et al. (2014); Qin et al. (2021)
PH	HELIOS-K/ExoMol	RT/TS	LaTY	Langleben et al. (2019)
PH ₃	DACE/ExoMol	RT/TS	SAITY	Sousa-Silva et al. (2015)
PO	DACE/ExoMol	RT/TS	POPS	Prajapat et al. (2017)
PS	HELIOS-K/ExoMol	RT/TS	POPS	Prajapat et al. (2017)
S	DACE	RT	VALD	Ryabchikova et al. (2015)

Each column gives source linelist, use and the reference for the opacities used in the radiative transfer(RT)/ transmission spectrum (TS). The RT opacities are as in Zilinskas et al. (2023). The TS opacities are PETITRADTRANS opacities.

Table A2. Opacities

Species	Source	use	Line list	Line List Reference
Si	DACE/ExoMOL	RT/TS	VALD/Kurucz	Ryabchikova et al. (2015); Kurucz (1992)
SiH	HELIOS-K/ExoMOL	RT/TS	Sightly	Yurchenko et al. (2018a)
SiH ₂	HELIOS-K/ExoMOL	RT/TS	CATS	Clark et al. (2020)
SiH ₄	DACE/ExoMOL	RT/TS	OY2T	Owens et al. (2017)
SiO	HELIOS-K/ExoMOL	RT/TS	SiOUVenIR	Yurchenko et al. (2022)
SiO ₂	DACE/ExoMOL	RT/TS	OYT3	Owens et al. (2020)
SiS	DACE/ExoMOL	RT/TS	UCTY	Upadhyay et al. (2018)
SiN	DACE	RT/TS	SiNfull	Semenov et al. (2022)
SO	DACE/ExoMOL	RT/TS	SOLIS	Brady et al. (2024)
SO ₂	ExoMOL	RT/TS	ExoAmes	Underwood et al. (2016a)
SO ₃	ExoMOL	RT	UYT2	Underwood et al. (2016b)
Ti	DACE/ExoMOL	RT/TS	VALD/Kurucz	Ryabchikova et al. (2015); Kurucz (1992)
TiH	HELIOS-K/ExoMOL	RT/TS	MoLLIST	Burrows et al. (2005); Bernath (2020)
TiO	HELIOS-K/ExoMOL	RT/TS	Toto	McKemmish et al. (2019)
COS	ExoMOL	TS	OYT8	Owens et al. (2024)
PN	ExoMOL	RT/TS	PaiN	Semenov et al. (2025)
O ₂	DACE/ExoMOL	RT/TS	HITRAN	Chubb et al. (2020)
O	DACE/ExoMOL	RT/TS	Kurucz	Kurucz (1992)
O ₂ , CO ₂ , CO, N ₂		RT/TS	Scattering	
H ₂ , H ₂ O, H, CH ₄		RT/TS	Scattering	
H ⁻		RT/TS	Continuum (bf & ff)	John (1988), Gray (2008)
H ₂ -H ₂	PETITRADTRANS	RT/TS	CIA	Borysow et al. (2001); Borysow (2002)
O ₂ -O ₂	PETITRADTRANS	TS	CIA	Karman et al. (2019)
N ₂ -H ₂	PETITRADTRANS	TS	CIA	Karman et al. (2019)
N ₂ -He	PETITRADTRANS	TS	CIA	Karman et al. (2019)
H ₂ O-N ₂	PETITRADTRANS	TS	CIA	Kofman & Villanueva (2021)
H ₂ O-H ₂ O	PETITRADTRANS	TS	CIA	Kofman & Villanueva (2021)

Each column gives source linelist, use and the reference for the opacities used in the radiative transfer(RT)/ transmission spectrum (TS). The RT opacities are as in [Zilinskas et al. \(2023\)](#). The TS opacities are PETITRADTRANS opacities.